



**HAL**  
open science

## Flux Emergence in a Magnetized Convection Zone

R.F. Pinto, A.S. Brun

► **To cite this version:**

R.F. Pinto, A.S. Brun. Flux Emergence in a Magnetized Convection Zone. The Astrophysical Journal, 2013, 772 (1), pp.55. 10.1088/0004-637X/772/1/55 . cea-00993745

**HAL Id: cea-00993745**

**<https://cea.hal.science/cea-00993745>**

Submitted on 15 Oct 2019

**HAL** is a multi-disciplinary open access archive for the deposit and dissemination of scientific research documents, whether they are published or not. The documents may come from teaching and research institutions in France or abroad, or from public or private research centers.

L'archive ouverte pluridisciplinaire **HAL**, est destinée au dépôt et à la diffusion de documents scientifiques de niveau recherche, publiés ou non, émanant des établissements d'enseignement et de recherche français ou étrangers, des laboratoires publics ou privés.

## FLUX EMERGENCE IN A MAGNETIZED CONVECTION ZONE

R. F. PINTO<sup>1</sup> AND A. S. BRUN

Laboratoire AIM Paris-Saclay, CEA/Irfu Université Paris-Diderot CNRS/INSU, F-91191 Gif-sur-Yvette, France; [ruipinto@cea.fr](mailto:ruipinto@cea.fr)

Received 2012 September 22; accepted 2013 May 8; published 2013 July 5

### ABSTRACT

We study the influence of a dynamo magnetic field on the buoyant rise and emergence of twisted magnetic flux ropes and their influence on the global external magnetic field. We ran three-dimensional MHD numerical simulations using the ASH code (anelastic spherical harmonics) and analyzed the dynamical evolution of such buoyant flux ropes from the bottom of the convection zone until the post-emergence phases. The global nature of this model can only very crudely and inaccurately represent the local dynamics of the buoyant rise of the implanted magnetic structure, but nonetheless allows us to study the influence of global effects, such as self-consistently generated differential rotation and meridional circulation, and of Coriolis forces. Although motivated by the solar context, this model cannot be thought of as a realistic model of the rise of magnetic structures and their emergence in the Sun, where the local dynamics are completely different. The properties of initial phases of the buoyant rise are determined essentially by the flux-rope's properties and the convective flows and consequently are in good agreement with previous studies. However, the effects of the interaction of the background dynamo field become increasingly strong as the flux ropes evolve. During the buoyant rise across the convection zone, the flux-rope's magnetic field strength scales as  $B \propto \rho^\alpha$ , with  $\alpha \lesssim 1$ . An increase of radial velocity, density, and current density is observed to precede flux emergence at all longitudes. The geometry, latitude, and relative orientation of the flux ropes with respect to the background magnetic field influences the resulting rise speeds, zonal flow amplitudes (which develop within the flux ropes), and the corresponding surface signatures. This influences the morphology, duration and amplitude of the surface shearing, and the Poynting flux associated with magnetic flux-rope emergence. The emerged magnetic flux influences the system's global polarity, leading in some cases to a polarity reversal while inhibiting the background dynamo from doing so in others. The emerged magnetic flux is slowly advected poleward while being diffused and assimilated by the background dynamo field.

*Key words:* Sun: dynamo – Sun: interior – Sun: surface magnetism

*Online-only material:* color figures

### 1. INTRODUCTION

It is well known that the Sun undergoes recurrent phases of intense magnetic activity. The most visible signature of magnetic activity is the presence of sunspots and active regions (ARs). These correspond to particularly strong concentrations of magnetic field that cross the surface of the Sun as a consequence of the underlying magnetoconvective dynamics and the flux-emergence phenomena in combination. Flux emergence occurs, nevertheless, at a very broad range of spatial and temporal scales, with the sunspots contributing to only a fraction of the total photospheric magnetic flux (Schrijver et al. 1997). The ARs are often composed of a mixture of large (unipolar) spots and small-scale polarities, which have a broad distribution of lifetimes ranging from days up to two solar rotation periods. During this period of time, they are observed to rotate and have their main polarity pairs separate, giving rise to more complex and dynamic polarity distributions. These magnetic structures are believed to be the surface tracers of twisted magnetic flux ropes generated further below (at the tachocline) that rise buoyantly up to the surface. They then emerge (at least partially) through the photosphere and provide the strong and coherent magnetic field structures composing the solar AR, which are prone to host eruptive events in the solar corona. Such events are likely to involve the surface convection, coronal dynamics, flux rope, and coronal magnetic flux. Furthermore, it is now becoming clear that

localized magnetic flux emergence is influenced by the large-scale magnetic field structure. Emergence events feed magnetic flux into the corona and may lead to important reconfigurations of its magnetic field, either in a quasi-steady or in an impulsive way (e.g., Liu et al. 2012). Conversely, the triggering of flares (or even coronal mass ejections) depends to a certain extent on the interaction of AR magnetic fields with their surroundings, namely on the orientation and gradients of the coronal field (Shibata et al. 1989; Forbes 2000; Kusano et al. 2012). Recent *SDO* (*Solar Dynamics Observatory*) observations indicate that flux emergence in one location can indeed trigger eruptive events in very distant parts of the solar surface (Schrijver & Title 2011). This emphasizes the idea that some of the physical processes relating to flux emergence are global in nature. The causal link between such seemingly independent events remains illusive and calls for the use of global-scale analysis.

The Sun has been going through its activity cycle for thousands of years, as revealed, for instance, by the modulation of the <sup>10</sup>Be concentration in Earth's polar ice cores (Beer et al. 1998). These cycles show a quasi-regular 11 yr period (22 if one distinguishes between opposite polarities of the Sun's global magnetic field), with the rising phase taking a shorter period of time than the decaying phase (DeRosa et al. 2012). There are some cycle-to-cycle variations (duration and intensity). For example, cycle 23 was longer than usual, with several months of unspotted solar surface between 2007 and 2009. Large sunspots and complex ARs are now regularly appearing as cycle 24 becomes stronger. Sunspots appearing more frequently during the rising phase of the cycle and at the activity maximum

<sup>1</sup> Now at LESIA, Observatoire de Paris, 5, Place Jules Janssen 92195 Meudon, France

contribute to the renewal of the coronal field and the global polarity reversal (Leighton 1969; Wang & Sheeley 1991).

Understanding the physics behind this wealth of inter-related phenomena certainly is a challenging affair. Numerical MHD simulations have been employed recurrently as a tool to model different aspects of the general flux-rope rise and emergence problem. The buoyant twisted flux ropes are generally believed to arise from the tachocline (or nearby) as a result of hydro-magnetic instabilities taking place there. These have been studied using mostly numerical models with local setups aiming specifically to resolve as much as possible the small-scale processes involved. A remarkable exception is the work by Nelson et al. (2011, 2013), who were able to produce self-consistently several buoyant toroidal structures that developed into omega loops in a fast-rotating convection zone (three times the solar rotation rate). Their breakthrough relied partly on the implementation of a numerical spatial scheme for the diffusive terms that allowed them to artificially reach substantially higher Reynolds and magnetic Reynolds numbers than they could have otherwise.

Kinematic dynamo models (e.g., Cameron & Schüssler 2007; Jouve et al. 2008) have been shown to be able to reproduce the long timescale properties of the global magnetic fields (the “butterfly diagram,” Jouve & Brun 2007; Charbonneau 2010) and predict, to some extent, the latitudes and times of sunspot formation (Işık et al. 2011; Nandy et al. 2011; Cameron & Schüssler 2007, 2012), but without accounting for the detailed magnetoconvective dynamics.

The study of the late phases of the buoyant rise and emergence of magnetic flux ropes has also resorted mostly to local high-resolution settings (e.g., Archontis & Hood 2010; Aulanier et al. 2005; Cheung et al. 2009; Linton et al. 1996; Archontis et al. 2005; Cheung et al. 2010; Hood & Priest 1979; Komm et al. 2011; Galsgaard & Nordlund 1997; Martínez-Sykora et al. 2008, 2009). These studies use simulation domains that typically span a few megameters above and below the photosphere. Such simulations attempt to describe the very strongly stratified photospheric layers as finely as possible, which justifies in most cases the use of high-resolution local simulation domains. One or multiple buoyant twisted magnetic flux ropes are introduced near the lower boundary (typically a few megameters below the surface) and evolve in more or less turbulent media until they emerge. For a more detailed discussion of local flux emergence, see the review by Fan (2009). Some of these works have been very successful at reproducing features observed at the surface of the Sun, but neglect (or strongly simplify) the constraints imposed by the large-scale dynamics. The global background dynamo and magnetoconvective processes at the origin of the large-scale meridional and zonal flows cannot be fully taken into account by this type of model.

The properties of the buoyant rise of magnetic flux ropes down from their assumed generation site up to the surface of the Sun require, to some extent, the use of global models of the convective zone. Studies based on the thin flux-tube approximation (Weber et al. 2011, 2012, among many others) allow one to follow the evolution of slowly buoyant tubes for very long timescales at the expense of neglecting all sources of magnetic or dynamical erosion caused by the background flows. Global simulations resorting to finite-width magnetic flux ropes, conversely, can take into account the interaction between the tube and the background convective motions and associated mean flows. They are nevertheless restricted to moderate Reynolds numbers and to the study of sufficiently strong flux ropes (as

the buoyant rise time needs to be considerably shorter than the diffusive timescales). The limits of the global approach can, in principle, be explored in more detail by resorting to local setups reaching higher spatial resolutions and hence higher Reynolds numbers (e.g., Hughes & Falle 1998). But these cannot capture the effects of the large-scale flows on the trajectories of such flux ropes, nor can they self-consistently quantify the angular momentum transport phenomena related to the rise of such coherent and presumably self-connected structures. The different approaches briefly listed in this paragraph are complementary and supply different pieces of the puzzle. There are two main options: (1) study local models that embed a large-scale magnetic structure in a highly turbulent flow; or (2) study global models that embed a large-scale magnetic structure in a large-scale, laminar (or weakly turbulent) flow. In the former, the magnetic structures feel a more realistic (relative to the solar case) bombardment by small-scale turbulence, but the disadvantage is that self-consistent large-scale fluid motions and large-scale background magnetic fields are omitted (although non-self-consistent versions could be added, e.g., Dorch 2007). The latter has the advantage that such large-scale effects can be included self-consistently. However, the numerical restrictions that the global geometry imposes only allow the study of the rise of the magnetic structure in a laminar or weakly turbulent flow, where magnetic structure and velocity scales are comparable and diffusion, advection, and transport times are all similar, thereby simulating a completely different problem from that encountered in the solar situation. We deliberately chose the latter option, as did Jouve & Brun (2009), to which this paper is meant to be compared.

Jouve & Brun (2009; hereafter JB09) specifically considered the influence of the global convective dynamics on the evolution of finite-width buoyant magnetic flux ropes. They performed a series of simulations of individual twisted magnetic flux ropes inside a spherical convection zone possessing both large-scale mean flows (e.g., solar-like differential rotation and meridional circulation) and fully developed hydrodynamical convection. They found that indeed latitudinal and longitudinal modulation of convective patterns and large-scale flows have a direct influence on the flux emergence of toroidal magnetic structures that are below  $6 - 7 B_{\text{eq}} \sim 4 \times 10^5 \text{ G}$ , where  $B_{\text{eq}}$  has been evaluated by computing the kinetic energy (KE) of the strongest downflows. Above such a threshold, the structures tend to rise and emerge almost as if they were embedded in a purely isentropic layer. In such global-scale convective simulations, the differential rotation was also found to influence the rise trajectory of the flux ropes. As in Wissink et al. (2000) and Abbett et al. (2001), the inertial (Coriolis) forces due to the flux-rope displacement have an azimuthal component and a (secondary) component pointing toward the rotation axis, which opposes the buoyant force (reducing its radial rise speed) and pushes the flux rope poleward. In JB09, the amplitude of this effect depends on the latitude at which the flux ropes are initially placed, and more specifically on the differential rotation profile at that latitude. They found that a solar-like background differential rotation makes flux-rope emergence more difficult at low latitudes. They further confirmed the existence of thresholds for the amount of twist and initial field amplitude to obtain a radial rise of uniformly buoyant magnetic structures.

The goal of this paper is to continue this effort by studying the evolution of twisted magnetic flux ropes in a fully magnetized three-dimensional convection zone with a background magnetic

field generated self-consistently by dynamo processes. We will thus focus on the large-scale effects rather than the small-scale turbulent processes involved. We introduce such twisted structures at the bottom of a magnetized turbulent convection zone and let it evolve for a long period of time—a few times longer than that of the buoyant rise timescale. This allows us to investigate whether and by what means the background magnetic field has an influence on the evolution of the coherent magnetic flux ropes. We note that while it might have been easier to impose a simpler steady global magnetic background field (as in Dorch 2007), we believe that only a time-varying multi-scale field as developed by dynamo action properly captures the dynamics involved in the issues we address here. We also address the importance of the buoyant rise and emergence of such flux ropes on the global energy and magnetic flux budgets. Furthermore, we explore whether surface diagnostics (evaluated at the top of the numerical domain), which precede and accompany the emergence of magnetic flux ropes, depend on the properties of the background field (Wang & Sheeley 1991; Schrijver & DeRosa 2003; Işık et al. 2011; Benevolenskaya 2004).

The remainder of this manuscript is organized as follows: Section 2 describes the model equations and numerical setup and discusses the parameter space explored and the scope and limitations of our model. Section 3 describes the early phases of the evolution of the twisted flux ropes (namely, the buoyant rise through the convection zone, CZ), Section 4 describes the flux-emergence phases, Section 5.1 describes the later phases (post-emergence and re-assimilation), and Section 5.2 discusses the consequences of the flux-emergence episodes in the corona. A general discussion follows in Section 6.

## 2. MODEL SETUP

### 2.1. Anelastic MHD Equations

The simulations described here were performed with the anelastic spherical harmonic (ASH) code. ASH solves the three-dimensional MHD anelastic equations of motion in a rotating spherical shell using a pseudo-spectral semi-implicit approach (Clune et al. 1999; Brun et al. 2004). The effects of compressibility on the convection are taken into account by means of the anelastic approximation, which correctly describes the advective dynamics while filtering out sound waves that would otherwise severely limit the time steps allowed by the simulation. ASH also uses a large-eddy simulation (LES) approach, with parameterization to account for subgrid-scale (SGS) motions. These equations are fully nonlinear in velocity and magnetic fields. The thermodynamic variables are linearized with respect to a spherically symmetric mean state with density  $\bar{\rho}$ , pressure  $\bar{P}$ , temperature  $\bar{T}$ , and specific entropy  $\bar{S}$ . Perturbations are denoted as  $\rho$ ,  $P$ ,  $T$ , and  $S$ . The equations being solved are

$$\nabla \cdot (\bar{\rho} \mathbf{v}) = 0, \quad (1)$$

$$\nabla \cdot \mathbf{B} = 0, \quad (2)$$

$$\begin{aligned} \bar{\rho} \left[ \frac{\partial \mathbf{v}}{\partial t} + (\mathbf{v} \cdot \nabla) \mathbf{v} + 2\Omega_0 \times \mathbf{v} \right] = -\nabla P + \rho \mathbf{g} \\ + \frac{1}{4\pi} (\nabla \times \mathbf{B}) \times \mathbf{B} - \nabla \cdot \mathcal{D} - [\nabla \bar{P} - \bar{\rho} \mathbf{g}], \end{aligned} \quad (3)$$

$$\begin{aligned} \bar{\rho} \bar{T} \frac{\partial S}{\partial t} + \bar{\rho} \bar{T} \mathbf{v} \cdot \nabla (\bar{S} + S) = \nabla \cdot [\kappa_r \bar{\rho} c_p \nabla (\bar{T} + T) \\ + \kappa_0 \bar{\rho} \bar{T} \nabla \bar{S} + \kappa \bar{\rho} \bar{T} \nabla S] + \frac{4\pi \eta}{c^2} \mathbf{j}^2 \\ + 2\bar{\rho} \nu \left[ e_{ij} e_{ij} - \frac{1}{3} (\nabla \cdot \mathbf{v})^2 \right], \end{aligned} \quad (4)$$

$$\frac{\partial \mathbf{B}}{\partial t} = \nabla \times (\mathbf{v} \times \mathbf{B}) - \nabla \times (\eta \nabla \times \mathbf{B}), \quad (5)$$

where  $c_p$  is the specific heat at constant pressure,  $\mathbf{v} = (v_r, v_\theta, v_\phi)$  is the local velocity in spherical geometry in the rotating frame of constant angular velocity  $\Omega_0 = \Omega_0 \hat{\mathbf{e}}_z$ ,  $\mathbf{B} = (B_r, B_\theta, B_\phi)$  is the magnetic field,  $\mathbf{j} = \frac{c}{4\pi} \nabla \times \mathbf{B}$  is the current density,  $\mathbf{g}$  is the gravitational acceleration,  $\kappa_r$  is the radiative diffusivity, and  $\mathcal{D}$  is the viscous stress tensor with components

$$\mathcal{D}_{ij} = -2\bar{\rho} \nu \left[ e_{ij} - \frac{1}{3} (\nabla \cdot \mathbf{v}) \delta_{ij} \right], \quad (6)$$

where  $e_{ij}$  is the strain rate tensor. As mentioned above, the ASH code uses an LES formulation where  $\nu$ ,  $\kappa$ , and  $\eta$  are assumed to be, respectively, an effective eddy viscosity, an eddy diffusivity, and a magnetic diffusivity (chosen to accommodate the resolution) that represent unresolved SGS processes. The thermal diffusion  $\kappa_0$  acting on the mean entropy gradient occupies a narrow region in the upper convection zone. Its purpose is to transport heat through the outer surface where radial convective motions vanish (Gilman & Glatzmaier 1981; Wong & Lilly 1994). To close the set of equations, linearized relations for the thermodynamic fluctuations are taken as

$$\frac{\rho}{\bar{\rho}} = \frac{P}{\bar{P}} - \frac{T}{\bar{T}} = \frac{P}{\gamma \bar{P}} - \frac{S}{c_p}. \quad (7)$$

This assumes the ideal gas law

$$\bar{P} = \mathcal{R} \bar{\rho} \bar{T}, \quad (8)$$

where  $\mathcal{R}$  is the ideal gas constant, taking into account the mean molecular weight  $\mu$  corresponding to a mixture composed roughly of three-fourths hydrogen and one-fourth helium per mass. The reference or mean state (indicated by overbars) is derived from a one-dimensional solar structure model and is regularly updated with the spherically symmetric components of the thermodynamic fluctuations as the simulation proceeds (Brun et al. 2002). It begins in hydrostatic balance, so the bracketed term on the right-hand side of Equation (3) initially vanishes. However, as the simulation evolves, both the turbulent and magnetic pressures drive the reference state slightly away from strict hydrostatic balance.

Finally, the boundary conditions for the velocity are impenetrable and stress-free at the top and bottom of the shell. We impose a constant radial entropy gradient at the top and bottom. A latitudinal entropy profile is imposed at the bottom, as in Miesch et al. (2006). We match the magnetic field to an external potential magnetic field both at the top and the bottom of the shell (Brun et al. 2004).

### 2.2. Background Dynamo Model

Our experiments consist of introducing a toroidal magnetic flux rope at the base of the convection zone in a thermally

**Table 1**  
Summary of the Background Dynamo Parameters

Domain	$0.72\text{--}0.97 R_{\odot}$
Grid resolution ( $N_r \times N_{\theta} \times N_{\phi}$ )	$256 \times 1024 \times 2048$
Diffusive coefficients (mid-CZ)	$\nu = 1.13 \times 10^{12} \text{ cm}^2 \text{ s}^{-1}$
	$\kappa = 4.53 \times 10^{12} \text{ cm}^2 \text{ s}^{-1}$
	$\eta = 2.83 \times 10^{11} \text{ cm}^2 \text{ s}^{-1}$
Dimensionless numbers	$P_r = 0.25, P_m = 4$
	$Ra = 1.85 \times 10^5 > Ra_c$
	$Re = 120, R_m \sim 480$
	$T_a = 1.8 \times 10^6, R_{oc} = 0.63$

**Notes.**  $\nu$ ,  $\kappa$ , and  $\eta$  are the effective viscosity, thermal diffusivity, and magnetic diffusivity.  $P_r$  and  $P_m$  are the Prandtl and magnetic Prandtl numbers.  $Ra$  and  $Ra_c$  are the Rayleigh and critical Rayleigh numbers.  $Re$  and  $R_m$  are the Reynolds and magnetic Reynolds numbers.  $T_a$  and  $R_{oc}$  are the Taylor and convective Rossby numbers. See Section 2.2 for more details.

equilibrated convection model in which a dynamo is operating. The study of the purely hydrodynamic case was the subject of JB09.

Our numerical model presents a simplified description of the physical processes acting on the magnetized solar convection zone. Solar values are taken for the heat flux, rotation rate, mass, and radius, and a perfect gas is assumed since the upper boundary of the shell lies below the H and He ionization zones. Contact is made with a seismically calibrated one-dimensional solar structure model for the radial stratification. Table 1 summarizes the model's main parameters, which we describe in detail below. The computational domain extends from about  $0.72 R_{\odot}$  to  $0.97 R_{\odot}$ . The numerical domain uses 256 grid points in the radial direction, 1024 in the latitudinal direction, and 2048 in azimuth. The reference state was obtained through the one-dimensional CESAM stellar evolution code (Morel 1997; Brun et al. 2002), which uses a classical mixing-length treatment calibrated on solar models to compute convection. We consider the central portion of the convection zone, while the penetrative convection below that zone and the atmosphere above (which is stable with respect to convection) are not taken into account. See Browning et al. (2006), Brun et al. (2011), Pinto & Brun (2011), and Warnecke et al. (2012) for simulations of solar convection coupled to lower and upper stable layers.

The effective viscosity, thermal diffusivity, and magnetic diffusivity  $\nu$ ,  $\kappa$ , and  $\eta$  are here taken to be functions of radius alone and are chosen to scale as the inverse of  $\bar{\rho}^{1/3}$ . We use the values  $\nu = 1.13 \times 10^{12} \text{ cm}^2 \text{ s}^{-1}$ ,  $\kappa = 4.53 \times 10^{12} \text{ cm}^2 \text{ s}^{-1}$ , and  $\eta = 2.83 \times 10^{11} \text{ cm}^2 \text{ s}^{-1}$  at mid-CZ, corresponding to a Prandtl number  $P_r = 0.25$  and a magnetic Prandtl number  $P_m = 4$ . The diffusive coefficients are, inevitably, much higher than those believed to represent the real solar conditions. The  $P_m$  value stated above is, consequently, considerably higher than the solar one, but eases the development of a sustained dynamo. The magnetic Prandtl number is held fixed in all the runs described in this manuscript. In all cases, the spherical shell is initially rotating at the rate  $\Omega_0 = 2.6 \times 10^{-6} \text{ rad s}^{-1}$  (corresponding to a rotation period of 28 days).

We start from a spherically symmetric convection zone with a realistic density stratification profile and solid-body rotation. The density contrast in this convective case is about 24 between the top and the bottom of the domain. The convection zone is initially in hydrostatic equilibrium but convection is readily triggered, as the background plasma is convectively unstable. The entropy gradient is  $dS/dr = -10^{-7}$ , and the Rayleigh number was chosen to be supercritical  $Ra = 1.85 \times 10^5 > Ra_c$

(the critical Rayleigh number being  $Ra_c \sim 10^4$ ; Jones & Kuzanyan 2009). The system then relaxes (after about one viscous timescale or hundreds of convective overturning times) to a statistically stationary state with a well-balanced radial energy flux throughout the whole domain (see the bottom panel of Figure 2 of JB09). The convection is moderately turbulent, with an rms Reynolds number  $Re = v_{\text{conv}}(r_{\text{top}} - r_{\text{bot}})/\nu_{\text{midCZ}} = 120$ , where the characteristic length scale is chosen as the depth of the CZ and  $v_{\text{conv}} = 80 \text{ m s}^{-1}$ . In the simulations, the Taylor number is  $T_a = 1.8 \times 10^6$  and the convective Rossby number is then  $R_{oc} = Ra/(T_a P_r) = 0.63 < 1$ , thus ensuring a prograde differential rotation (Brun & Toomre 2002). Figure 1 displays the radial convective velocity along with the differential and meridional circulation achieved self-consistently in the simulation. As described in more detail in JB09, convection is dominated at low latitudes by elongated patterns (the so-called banana convective cells), whereas high-latitude convective patterns are more isotropic. We note at mid-latitude a zone of strong horizontal shear associated with the large axisymmetric differential rotation realized in the simulation. The radial and latitudinal profile of the angular velocity are solar-like when compared to helioseismic inversions (Schou et al. 1998; Thompson et al. 2003), with a fast equator, slow pole, and conical profile at mid-latitude. However, we acknowledge that we do not model the tachocline nor the near surface shear layer. For the former, we adopt the latitudinal thermal wind forcing used in Miesch et al. (2006; see Brun et al. 2011 for a more self-consistent approach). Finally, we also display the axisymmetric meridional flow present in the simulation. It is mostly poleward near the surface, with one large dominant cell on the order of  $20 \text{ m s}^{-1}$ . Small counter cells are also seen near the boundaries and in the polar cap, where azimuthal averages are harder to perform due to the small lever arm there.

Starting from such a hydrodynamical convective state, we then add a seed magnetic field that evolves by the action of the dynamo processes driven by the turbulent motions described above. A weak seed magnetic field was chosen to be a  $\{l = 5, m = 4\}$  multipole introduced in the convection zone. The system was then evolved for 800 days, or about 28 solar rotations. With our choice of parameters, the magnetic Reynolds number is  $R_m = Re \times P_m \sim 480$ . This is well above the threshold of about 300 for dynamo action in stratified and rotating solar convective shells, as evaluated by Brun et al. (2004). Figure 2 displays the ratio between magnetic energy (ME) and kinetic energy (KE) over the last 400 days of the simulation. We indeed see that dynamo action takes place, as ME/KE increases steadily. We clearly also see the exponential growth and the change of the slope when nonlinear feedback from the Lorentz force starts to be felt by the flow. We ran the simulation until ME reaches an amplitude on the order of 2% of KE. We chose to stop the simulation at that instant ( $t = 0$  day in the figure) as we did not want the averaged background field to be too intense and the large-scale axisymmetric flows to be influenced by the growing magnetic field. This somewhat arbitrary choice allows us to have a multi-scale background magnetic field while keeping the background large-scale flows unchanged, hence allowing us to establish a direct link with previous works (e.g., Jouve & Brun 2009). In particular, the differential rotation remains solar-like, similar to the one shown on Figure 1, since Maxwell stresses are not yet strong enough to modify significantly the redistribution of angular momentum (see Brun et al. 2004 for a more detailed discussion).

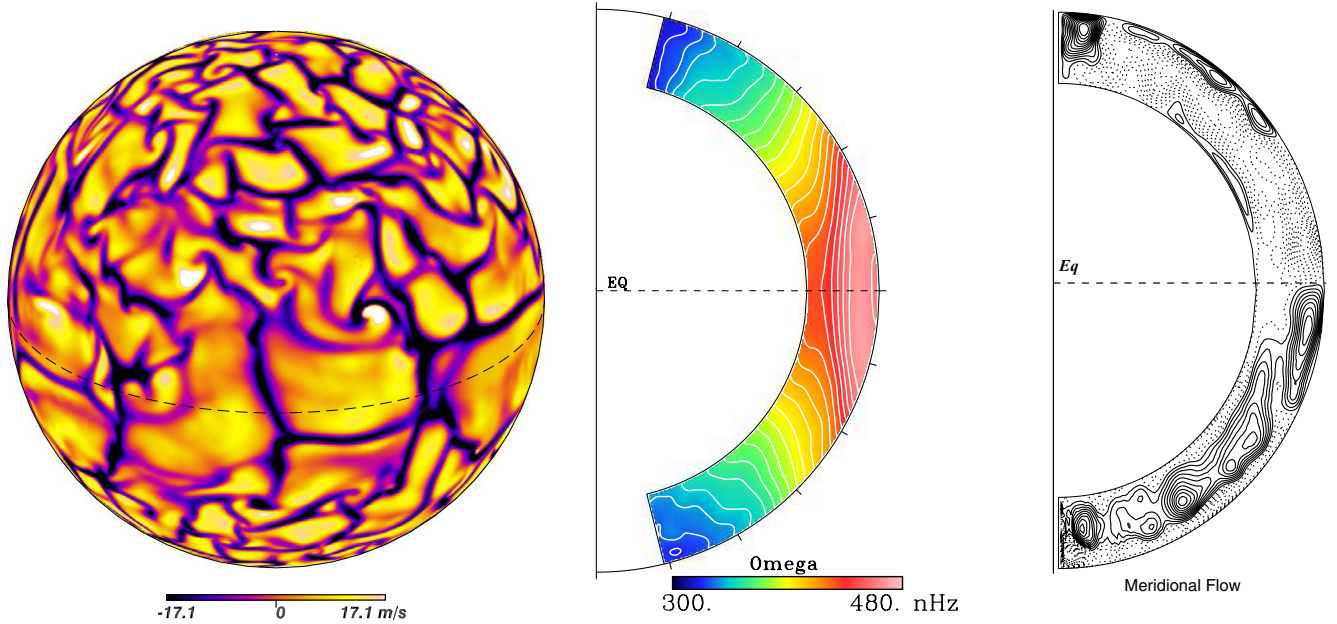


**Figure 1.** Convective motions and mean flows in our model. The left panel shows the radial velocity profile near the top of the shell, with yellow and dark blue tones representing, respectively, upflows and downflows. The middle panel shows the differential rotation profile, and the right panel shows the meridional circulation. The last two panels show longitude- and time-(272 days) averaged data. For the meridional flow, dashed (solid) lines represent counterclockwise (clockwise) circulation, and the intensity varies approximately between about  $-20$  and  $20 \text{ m s}^{-1}$ . (A color version of this figure is available in the online journal.)

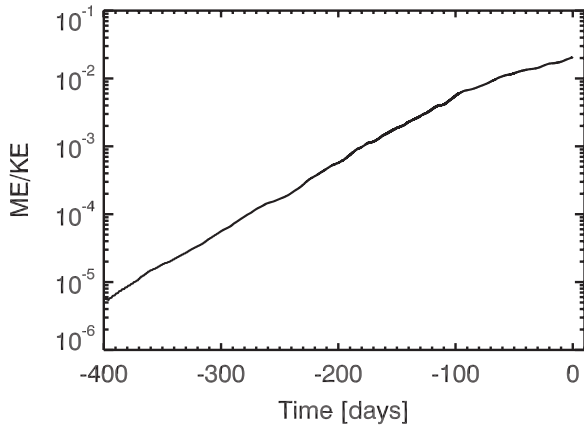


**Figure 2.** Evolution of the ratio of magnetic energy (ME) to kinetic energy (KE) for the background dynamo field. The instant  $t = 0$  corresponds to the introduction time of the magnetic flux rope.

In Figure 3, we show the surface radial magnetic field at  $t = 0$  day. This corresponds to the instant of introduction (addition to the background field) of our twisted magnetic flux ropes (see Section 2.3). As already discussed in Brun et al. (2004), the radial component of the field is mostly found in the downflow lanes and ME can locally be more intense than KE (see also Cattaneo 1999).

Figure 4 shows more precisely the distribution of the magnetic field's strength on the section of the CZ traversed by the flux ropes (see Section 2.3 for more details) at  $t = 0$ . The average background field amplitude is about  $0.7 \times 10^3 \text{ G}$ , and the upper tail of the distribution extends up to about  $5 \times 10^4 \text{ G}$ . In the region traversed by the magnetic flux ropes, the radial component of the magnetic field is on average slightly smaller than the horizontal components. To show this better, the bottom panel in Figure 4 displays the background magnetic field's pitch angle distribution

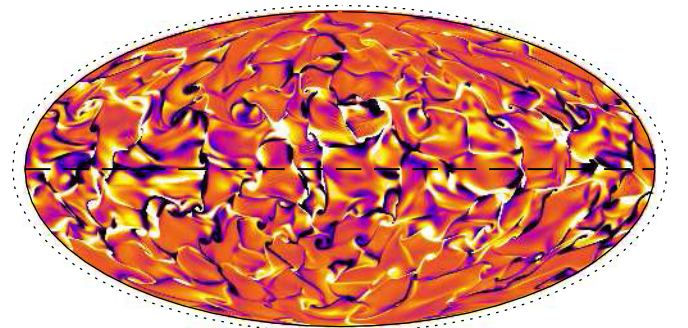


**Figure 3.** Mollweide projection of the radial component of the background dynamo magnetic field near  $r = 0.96R$  at  $t = 0$ . Dark tones denote negative polarity. The color table scales from  $-170$  to  $+170 \text{ G}$ . Note the presence of mixed field polarity in the downflow lanes. The dotted black line indicates the position of the spherical surface placed at  $r = 1 R_{\odot}$ . (A color version of this figure is available in the online journal.)

in the same sub-domain. The pitch angle  $\psi$  is defined here as the angle between the magnetic field vector and the azimuthal direction, such that

$$\tan \psi = \frac{\sqrt{B_r^2 + B_\theta^2}}{B_\phi}. \quad (9)$$

If the magnetic field vectors had random spatial orientations everywhere in the domain, then the probability distribution function (PDF) for the pitch angle  $f(\psi)$  would be such that

$$f(\psi) d\psi = \frac{2\pi B^2 |\sin \psi| d\psi}{4\pi B^2} = \frac{1}{2} |\sin \psi| d\psi. \quad (10)$$

The function  $f(\psi)$  is represented by the dashed line in the bottom panel of Figure 4. This shows that the background field is slightly more toroidal than poloidal in this region.

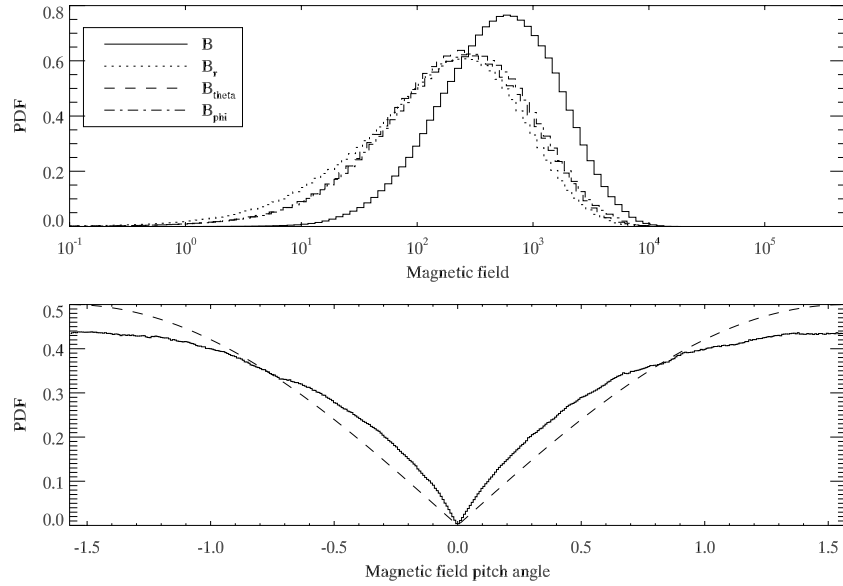


**Figure 4.** PDF of the magnetic field amplitude  $B = \sqrt{(B_r^2 + B_\theta^2 + B_\phi^2)}$  at  $t = 0$  in the latitudinal interval  $[25^\circ\text{N}, 45^\circ\text{N}]$  covered by the flux-rope’s evolution (top panel; note, all three  $\mathbf{B}$  components are superimposed). Note that the histogram bins are distributed logarithmically. The global dynamo field peaks between  $10^2$  G and  $10^3$  G and the FWHM of the distribution is of about one order of magnitude around that value. The bottom panel shows the PDF for the magnetic field’s pitch angle in the same latitudinal interval (thick continuous line) and the expected distribution for a uniform random distribution of poloidal and toroidal fields (thin dashed line).

**Table 2**  
Flux-rope Parameters for the Runs Discussed in the Text

Run	$B_\phi^{\max}$ ( $10^5$ G)	$A_0$ ( $10^3$ )	$q$	$A_s$
Standard flux rope	1.73	3.30	20	0.00
Negative flux rope	-1.73	-3.30	20	0.00
Left-handed flux rope	1.73	3.30	-20	0.00
Left-handed negative flux rope	-1.73	-3.30	-20	0.00
Weak flux rope	8.66	1.65	20	0.00
Medium flux rope	1.30	2.48	20	0.00
No dynamo, standard flux rope	1.73	3.30	20	52.3
High buoyancy, medium field	1.30	2.48	20	23.2
High buoyancy, weak field	8.66	1.65	20	23.2

For comparison purposes, we also prepared a purely hydrodynamical background with the same properties (stratification, meridional flows, and rotation pattern) as the dynamo runs but without a background magnetic field.

### 2.3. Introduction of a Flux Rope

We introduced axisymmetric toroidal twisted magnetic flux ropes near the lower boundary of the computational domain. The (background) initial conditions are those resulting from the evolution of a dynamo run, as presented above (Section 2.2). We performed several runs, whose parameters are listed in Table 2. Figure 5 shows the initial state of a typical run (our standard case).

The magnetic geometry of the flux rope is expressed by the two potential functions  $A$  and  $C$

$$A(r, \theta) = -A_0 r \times \delta(r, \theta), \quad (11)$$

$$C(r, \theta) = -\frac{A_0 a^2 q}{2} \times \delta(r, \theta), \quad (12)$$

where

$$\delta(r, \theta) = \exp\left[-\left(\frac{r - R_t}{a}\right)^2\right] \left[1 + \tanh\left(2\frac{\theta - \theta_t}{a/R_t}\right)\right].$$

These potential functions define a divergenceless and axisymmetric magnetic field  $\mathbf{B}$  in terms of the poloidal–toroidal decomposition

$$\mathbf{B} = \nabla \times \nabla \times (C \mathbf{e}_r) + \nabla \times (A \mathbf{e}_r), \quad (13)$$

amplitude of which at the axis of the structure ( $r = R_t$ ,  $\theta = \theta_t$ ) is given by

$$B_0 \equiv B_\phi^{\max} = 2A_0 \frac{R_t}{a}. \quad (14)$$

The pitch angle  $\psi$  of the twisted magnetic field lines with respect to the azimuthal direction at the flux-rope’s boundary is such that

$$\tan \psi \approx \frac{qa}{R_t + a}. \quad (15)$$

We also apply the following entropy perturbation to the background field:

$$\delta S = -A_s \frac{2R_t}{a} \exp\left[-\left(\frac{r - R_t}{a}\right)^2\right] \left[\cosh^2\left(2\frac{\theta - \theta_t}{a/R_t}\right)\right]^{-1}, \quad (16)$$

where its maximum amplitude is  $\Delta S = -2A_s R_t/a$  at the flux-rope’s axis. The flux ropes are initially setup in pressure equilibrium with the surrounding plasma. This condition constrains the density deficit  $\Delta\rho/\rho$  (relative to the background density) to

$$\frac{\Delta\rho}{\rho} = 1 - \exp\left[-\frac{\Delta S}{c_p}\right] \left[1 - \frac{B_0^2}{8\pi P}\right]^{1/\gamma}. \quad (17)$$

We only consider in this paper  $\delta(r, \theta)$  and  $\delta S$  perturbations, which are axisymmetric, such that the flux-rope buoyancy is independent of the azimuthal coordinate (unlike in Fan 2008; Jouve et al. 2013).

As shown by Emonet & Moreno-Insertis (1998), there is a threshold in magnetic twist that the flux rope must have in order to maintain its coherence during its rise through the convection

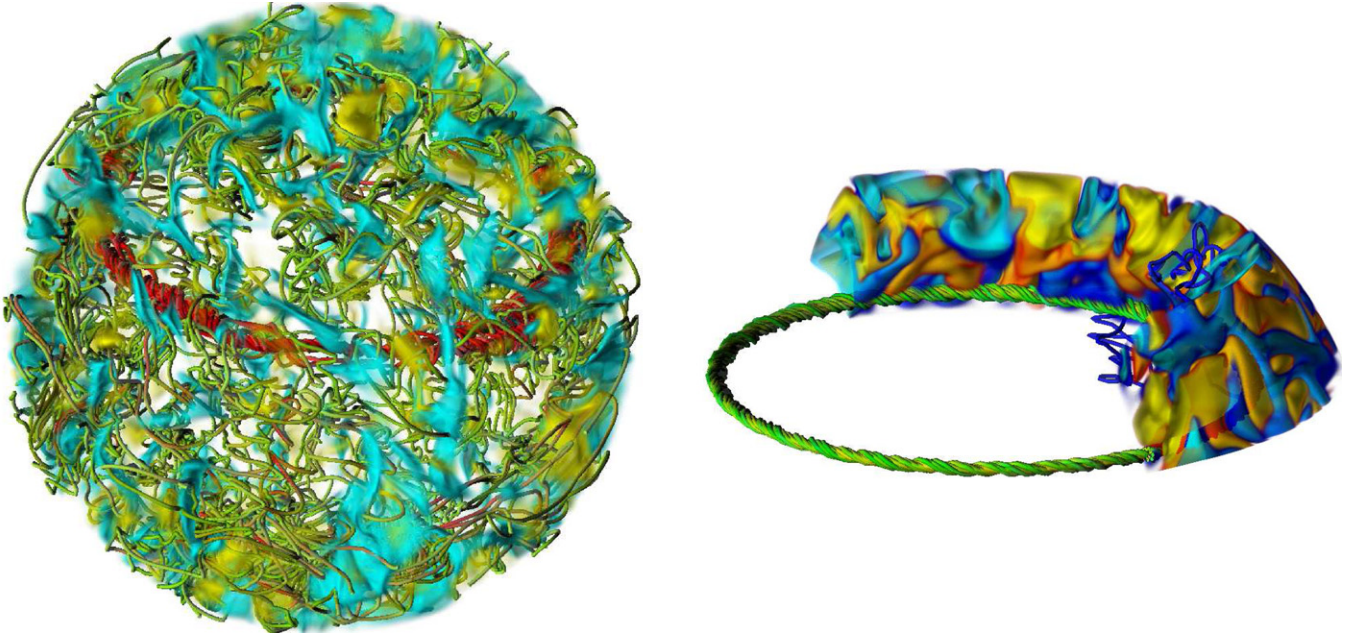


**Figure 5.** Initial conditions. Snapshot of a twisted magnetic flux rope introduced at the bottom of the CZ in the dynamo run described in Section 2.2. The left panel shows a sample of magnetic field lines from the entire numerical domain (for which red/green tones represent strong/weak  $\mathbf{B}$  field). The right panel shows the flux rope in more detail over a small sub-domain of the numerical setup. In both the panels, blue and yellow volumes represent, respectively, convective upflows and downflows (only the strongest down and upflows are represented on the left panel).

(A color version of this figure is available in the online journal.)

zone. This threshold is expressed in terms of a minimum pitch angle  $\psi$  at the tube's periphery

$$\sin \psi_t = \frac{|B_{\text{poloidal}}|}{\|\mathbf{B}\|} \geq \left[ \frac{a}{H_p} \left| \frac{\Delta\rho}{\bar{\rho}} \right| \frac{\beta}{2} \right]^{1/2}, \quad (18)$$

where  $a$  is the flux-rope's radius,  $H_p$  is the background pressure scale height,  $\Delta\rho$  is the density deficit relative to the background density  $\bar{\rho}$ , and  $\beta$  is the ratio of gas to magnetic pressures. In simple terms, a flux rope is able to rise cohesively if its magnetic tension is able to counteract the torque applied by the flows around the magnetic structure as it buoyantly rises. Equation (18) describes this balance in the plane orthogonal to the flux-rope's axis, which is to say the poloidal plane in an axisymmetric setup. The overall picture of the conditions for the cohesive rise of such flux ropes in three-dimensional convective shells was subject of previous studies (Archontis et al. 2005; Jouve & Brun 2009, among others). Detailed discussions of the evolution of twisted flux ropes near, above, and below this threshold can be found in Jouve & Brun (2009). Following those studies' conclusions, in this paper we will only consider magnetic structures that are expected to rise cohesively. The focus here is on how the globally magnetized medium, rather than a purely hydrodynamic one, interacts with and affects the evolution of these magnetic structures (as explained in Section 2.2).

Figure 6 shows the parameter space  $|B|$  versus  $\Delta S$  used to define the runs listed in Table 2 and summarizes the relations between all the flux-rope parameters. Contours of constant  $\Delta\rho/\rho$  (black continuous lines) and  $\sin \psi_t$  (blue dashed lines) were overplotted to show how the different runs relate to each other in terms of these two fundamental parameters. The density deficit  $\Delta\rho/\rho$  (and consequently, the buoyant rise speed) increases from left to right and from bottom to top. For a given  $B_0$ , a positive  $\Delta S$  translates into a density deficit higher than that in the  $\Delta S = 0$  case. The buoyant rise speed increases accordingly,

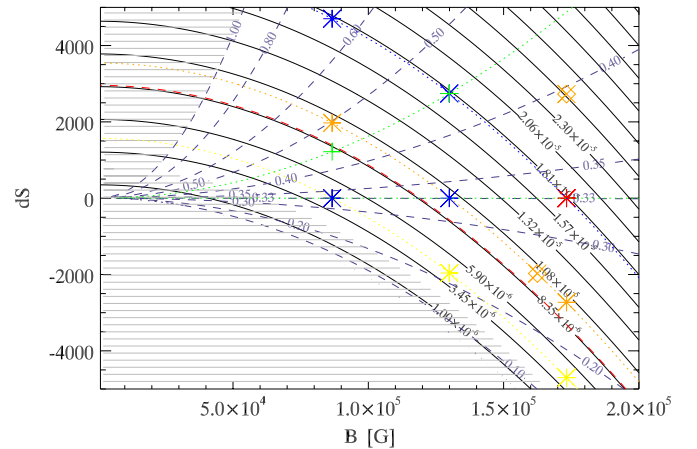


**Figure 6.** Flux-rope parameter space  $|B|$  vs.  $\Delta S$ . The continuous black lines are contours of the perturbation  $\Delta\rho/\rho$  at the center of the twisted flux ropes, which corresponds to a given pair  $\{|\mathbf{B}_0|, \Delta S\}$ . The blue dashed lines represent  $\sin \psi_t$ , where  $\psi_t$  is the twist threshold for a given flux rope. The filled regions (gray horizontal lines) are excluded a priori, corresponding to  $\sin \psi \geq 1$  or magnetic fields below the minimum field strength threshold ( $B = 6.1 \times 10^4$  G for  $\Delta S = 0$ ) found in Jouve & Brun (2009). The red dashed line represents an empirical re-evaluation of this threshold as an outcome of our simulations. The red asterisk represents our standard case. The dotted blue line follows the contour of constant  $\Delta\rho/\rho$ , which contains the standard case. The blue and red asterisks represent the cases that are more thoroughly discussed in this manuscript. The other symbols represent runs used to verify the consistency in our approach.

(A color version of this figure is available in the online journal.)

and the so does the corresponding threshold pitch angle  $\psi_t$ . A negative  $\Delta S$  produces the opposite effect. It is also possible to explore different flux-rope magnetic field strengths while keeping the same density deficit. Decreasing the magnetic field amplitude  $B_0$  then implies increasing  $\Delta S$ . This corresponds to an upward and leftward trajectory over one of the  $\Delta\rho/\rho$  contour lines in the plot, and therefore to an increase in the pitch

angle threshold. Indeed, torque balance in the meridional plane (or in the plane orthogonal to the flux-rope’s axis) requires that the flux ropes keep the same poloidal magnetic field amplitude if the buoyant driver remains the same (having all other parameters— $a$  and  $H_p$ —fixed). The only way to satisfy this condition while decreasing  $B_0$  is to increase the flux-rope’s pitch angle. Increasing the magnetic field amplitude  $B_0$  while keeping  $\Delta\rho/\rho$  constant has the opposite consequences; namely, this implies a decrease in  $\Delta S$  and pitch angle threshold  $\psi_t$ . The same type of reasoning can be applied to paths of constant  $\psi_t$  in the  $\{B_0, \Delta S\}$  parameter space. The areas of the parameter space for which it is impossible to form cohesive buoyant flux ropes are grayed out. These correspond specifically to  $\{B_0, \Delta S\}$  pairs that imply  $\sin \psi_t > 1$  and to density deficits not strong enough to counteract the strongest convective downflows in the CZ. We note that in practice the latter limit actually underestimates the minimum value for  $\Delta\rho/\rho$  that can be used. The red dashed line represents an empirical re-evaluation of the  $\Delta\rho/\rho$  threshold, as an outcome of our simulations. Very slowly rising buoyant flux-rope’s may require extremely low diffusivities, such that the corresponding diffusive timescales are larger than their long buoyant rise timescales. It is of course easier to follow numerically the evolution of strongly buoyant flux ropes than weakly buoyant ones (as the diffusive coefficients cannot be lowered arbitrarily), and our model presents no exception to this general rule.

For completeness, below we show the scaling relations between  $\Delta S$ ,  $B$ ,  $\Delta\rho/\rho$ , and  $\sin \psi_t$ , which follow from Equations (16)–(18):

$$\Delta S \left( \frac{\Delta\rho}{\rho}, B \right) = -c_p \ln \left[ 1 - \frac{\Delta\rho}{\rho} \right] + \frac{c_p}{\gamma} \ln \left[ 1 - \frac{B^2}{8\pi P} \right] \quad (19)$$

$$\frac{\Delta\rho}{\rho} (B, \psi_t) = \sin^2 \psi_t \left[ \frac{a}{H_p} \frac{4\pi P}{B^2} \right]^{-1} \quad (20)$$

$$\Delta S (B, \psi_t) = -c_p \ln \left[ 1 - \sin^2 \psi_t \left( \frac{a}{H_p} \frac{4\pi P}{B^2} \right) \right] + \frac{c_p}{\gamma} \ln \left[ 1 - \frac{B^2}{8\pi P} \right]. \quad (21)$$

Figure 6 was built assuming invariant  $a = 2.87 \times 10^{-2} R_\odot$  and  $R_t = 0.75 R_\odot$ , which are the ones we chose to use in our simulations. The values of  $P$ ,  $H_p$ , and  $c_p$  are then implicitly defined by the former parameters (the flux-rope’s initial position) and the convective background, and are therefore also invariant. Changing these would affect the exact slopes and positions of the  $\Delta\rho/\rho$  and  $\sin \psi_t$  contour lines, slightly deforming the diagram but still maintaining its main properties.

#### 2.4. Scope and Limits of Our Model

Let us better clarify the scope and limits of our methods before moving on to the more detailed discussion of our work. We use a global three-dimensional numerical model of a convective spherical shell that solves a set of MHD equations in the frame of the anelastic approximation (discussed in detail in Bannon 1996; Lantz & Fan 1999). The maximum numerical resolution we use (giving a spatial resolution of 1.5–2 Mm horizontally and 0.01–1 Mm vertically) restricts our studies to

laminar or weakly turbulent flows and large cross-sectional area flux ropes. The effective viscosity and resistivity are necessarily much higher than those in the real Sun, and our magnetic structures are resolved with about 64 points in radius and 25 points in latitude. Note that previous local studies have required at least 200 points in each direction (Fan 2008; Dorch 2007) and that some authors (e.g., Hughes & Falle 1998) argue that resolution and the local Reynolds numbers are critical to an accurate portrayal of the rise of a structure. The necessity of making the magnetic structure large in conjunction with high diffusivities leads to length scales and timescales of the convective flows and background magnetic fields that are comparable to those of the magnetic structure. The magnetic structures occupy approximately one-fourth of the convection zone by radius and evolve on a timescale of about 25 days, which may be compared with the convective turnover time of 35 days and the magnetic diffusion time of 80 days. Therefore, due to our choice of a global geometry and the constraints it places on numerical resolution, we are necessarily restricted to studying the brief rise of a large magnetic structure in a large-scale weakly turbulent magnetoconvective background where diffusive processes clearly play a significant role. This means that what we study is clearly not the solar problem, wherein a magnetic structure that is much larger than the typical length scales of both the highly turbulent velocity and magnetic fields rises quickly on a timescale that is far shorter than any diffusive timescale. Furthermore, the similarity of all our length scales demands that numerous realizations of the simulations be performed to create accurate statistics, but such a task is unfortunately too expensive to perform in our global geometry. Our magnetic background is also somewhat arbitrary. In our simulations, idealized twisted magnetic flux ropes are added to a magnetoconvective setup—a dynamo—which we let evolve 400 days beforehand. The ME spectrum reaches a fully developed profile after about 150 days, with the later evolution (between 150 and 400 days) translating simply into an increase of amplitude of the whole spectrum. We chose to stop the dynamo run when the ME reached about 2% of the KE. This deliberate but completely arbitrary choice ensures that the background flows retain the same global properties (meridional circulation and prograde differential rotation) and hence lets us establish a more clear comparison with the progenitor hydrodynamic case (Jouve & Brun 2009). Different background dynamo setups could perhaps lead to different results, and such effects should be addressed in the future. Furthermore, it should be noted that the top of the numerical domain (the “surface”) is placed at  $0.97 R_\odot$ , thereby omitting a very dynamic layer of the actual solar surface. Thus, our conclusions concerning “flux emergence” are strictly related to emergence from the weakly stratified interior of the calculation into the highly stratified surface convective layers above. Significant modification of any characteristics detected in our simulations should be expected, and therefore any predictions must be considered very carefully before any relation to the solar context is implied (as in Abbett et al. 2001, for example). However, due to the first point above, these simulations should in no way be considered as solar anyway.

### 3. BUOYANT RISE IN A DYNAMO FIELD

Let us now describe the evolution of the twisted magnetic flux ropes introduced near the bottom boundary of the background model described above (Section 2).

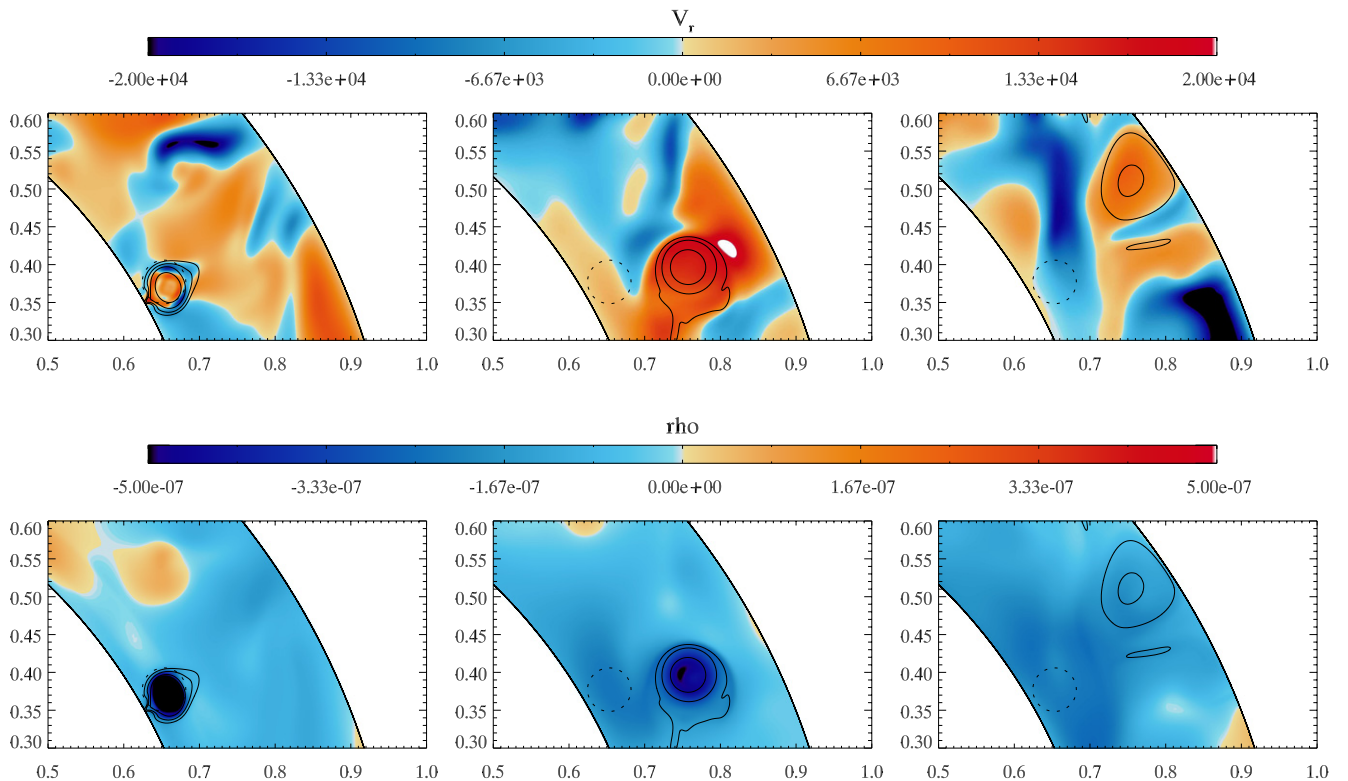


**Figure 7.** Sequence of snapshots of the flux rope in the standard case (polar slices at  $\phi = 90^\circ$ ) at three different moments in its temporal evolution ( $t \approx 1, 10,$  and  $20$  days). The color scale shows  $v_r$  in the top row and  $\Delta\rho$  in the bottom row. The axis coordinates are in units of  $R_\odot$ , with the origin at the center of the Sun. The black continuous lines are contours of  $B_\phi$ . The dotted line represents the initial position of the tube. (A color version of this figure is available in the online journal.)

### 3.1. Buoyant Rise Properties

Figure 7 shows three snapshots of the evolution of a flux rope as it rises through the convection zone, namely at  $t \approx 1, 10,$  and  $20$  days. The top row shows the radial velocity  $v_r$ , while the second row shows the density deficit  $\Delta\rho$  in the flux rope. The black lines are contours of the toroidal magnetic field  $B_\phi$ . For simplicity, only the standard case is represented in the figure (strong-field highly buoyant case). All other cases in which flux ropes manage to emerge share the same qualitative properties; the differences will be discussed later on in the text. The flux rope expands as it rises mostly due to the background pressure stratification and partially due to magnetic diffusion. We emphasize that the flux-rope’s diffusive timescale  $a^2/\eta$  is 80 days, which is longer than the typical buoyant rise time ( $\sim 10$  days, except for the very weakly buoyant cases). The flux-rope section is perfectly circular at  $t = 0$ , but its periphery suffers small and intermittent deformations. At about  $t = 1$  day, the buoyant force has provided enough upward momentum for the flux rope to start rising coherently. The top left panel in Figure 7 shows that the whole core of the flux rope has a positive  $v_r$  at this moment, while its periphery still shows a different (yet transient) behavior. The first panel in the second row in the figure depicts how the density deficit  $\Delta\rho$  (which the buoyant force is proportional to) is stronger at the core than at the periphery, partly explaining the aforementioned different behaviors (see also the definitions in Equations (11)–(17)). Also, the magnetic tension responsible for keeping the flux rope together against the work done by the external flows is weaker at its periphery, as the magnetic field strength is weaker there and field-line curvature radii are larger. The magnetic tension force in the poloidal plane scales as  $F_T \propto B_p^2/R_c$  for a flux-rope layer with a circular

cross-section, where  $R_c$  is the curvature radius and  $B_p$  is the poloidal magnetic field amplitude. The second panels in both rows of Figure 7 show the same flux rope close to mid-height in the convection zone. At this time ( $t \approx 10$  days), the flux-rope’s rise speed is close to its maximum value ( $\sim 115 \text{ m s}^{-1}$ ; see Figure 9). The core of the flux rope maintains its circular cross-section, which has expanded to a larger radius, and the density deficit  $\Delta\rho$  as decreased accordingly. It is worth noting that while the flux-rope’s periphery is continuously dragged with the surrounding flows, the well-known double-tailed profile is not clearly identified in the dynamo runs as it is in the case with a hydrodynamic background (cf., e.g., Emonet & Moreno-Insertis 1998; Hughes & Falle 1998; Jouve & Brun 2009, particularly the first panel in Figure 19 of the latter, for the case with  $P_m = 4$ ). In fact, a wake continuously forms behind the rising flux ropes, but it is promptly assimilated by the magnetic background field. (The magnetic field in the former and the latter are of the same magnitude.) The peripheral layers of the flux ropes show a rather erratic pattern in all runs with a dynamo background, suggesting magnetic flux is continuously exchanged with the magnetized surroundings. The third panel of Figure 7 shows the flux rope after it has reached the top boundary of the domain and stopped rising buoyantly. At the moment represented ( $t \approx 20$  days), the system has gone past a flux-emergence episode (see Section 4). The flux rope maintains its spatial coherence for a period of time much longer than the buoyant rise time, though. The flux rope remains in the highest layers of the CZ while being slowly advected poleward by the mean meridional flows and sheared by the horizontal surface flows (see Section 4.2 for details on the poleward drift and surface shearing). At the same time, a part of its magnetic flux progressively reconnects and mixes with the ambient magnetic

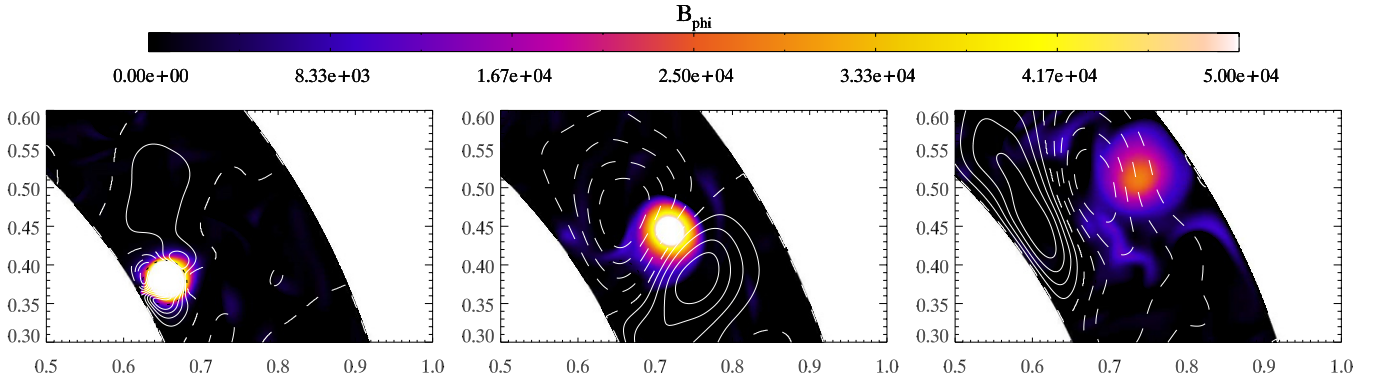


**Figure 8.** Sequence of snapshots (polar slices at  $\phi = 90^\circ$ ) at the same moments in temporal evolution as in Figure 7 ( $t \approx 1, 10,$  and  $20$  days) and in the same sub-domain. The color scale represents the amplitude of  $B_\phi$ , thus tracing the flux-rope’s position. The white lines are streamlines of the poloidal mass flux  $\rho v$  (i.e., contours of its stream function); the continuous lines represent CW flows; and the dashed lines represent CCW flows.

(A color version of this figure is available in the online journal.)

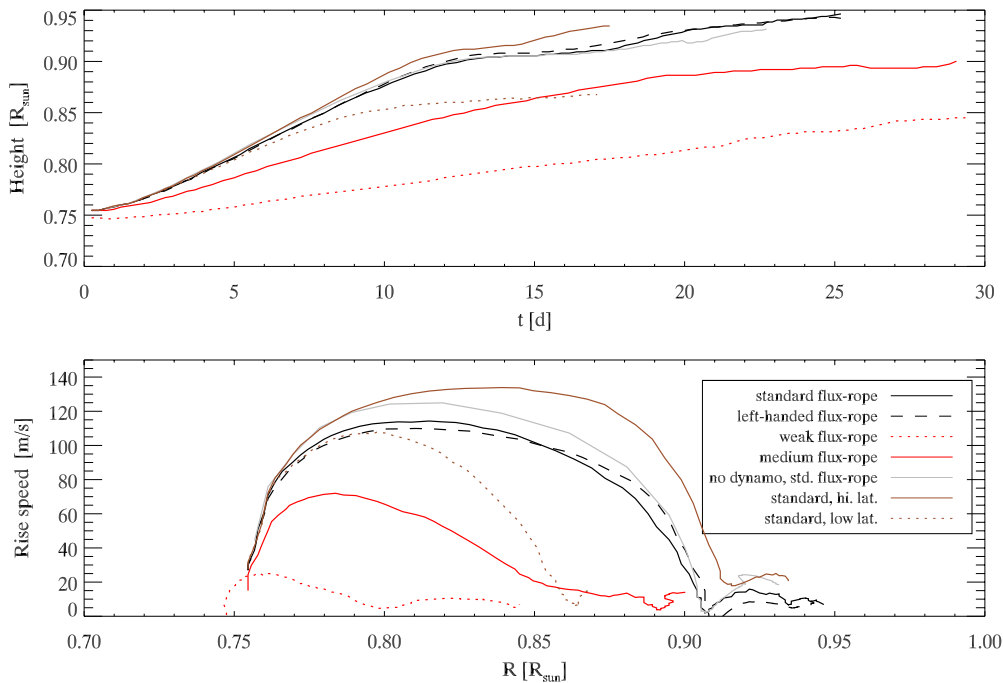


**Figure 9.** Height (radius) and rising velocity of the center of the magnetic flux rope. The axis of the flux rope is defined here as the position of the maximum of  $B_\phi$  in the meridional plane. Each curve corresponds to one of the runs listed in Table 2 (cf. the inset key for reference).

(A color version of this figure is available in the online journal.)

field. Section 5.1 describes in greater detail the later evolution phases. The flux rope generates a dipolar flow around itself as it rises buoyantly through the CZ, as shown in Figure 8. The color scale represents the toroidal field  $B_\phi$ , and the white lines are streamlines of the azimuthally averaged poloidal mass flux  $\bar{\rho} \langle \mathbf{v}_p \rangle_\phi$ . Dashed and continuous lines represent, respectively, counterclockwise (CCW) and clockwise (CW) circulations. The instants represented are the same as in Figure 7. This circulation flow has the following characteristics: a strong radially oriented upflow above the flux rope, a shallower upflow in the wake of the flux rope, and a return flow that encircles the flux rope. This flow pattern appears as soon as the flux rope starts rising buoyantly as a whole, as can be seen in the first panel ( $t \approx 1$  day). At this stage, the dipolar flow encompasses a small area with a radius roughly twice as big as that of the flux rope. The spatial extent of this pattern increases with time, as the flux-rope rise speed increases (and the flux-rope magnetic field is strong enough for it to keep its coherence). This is clear in the second panel

( $t \approx 10$  days), when the flux rope is close to its maximal rise speed. The dipolar flow is destroyed as the rope slows down when it reaches the surface (third panel,  $t \approx 20$  days).

### 3.2. Buoyant Rise Speed

Figure 9 shows the height of the flux-rope’s axis as a function of time (top panel) and its rising velocity as a function of radius (bottom panel) for the standard case (strong magnetic field), the case with a hydrodynamic background and a standard flux rope, the case with a left-handed flux rope, and the cases with intermediate and weak field and low buoyancy. We also considered low-latitude and high-latitude cases, corresponding to flux ropes similar to those in the standard case, but his time placed initially at  $15^\circ\text{N}$  and  $45^\circ\text{N}$ , respectively. Among the standard latitude cases, the flux rope evolving in a purely hydrodynamical background has the highest buoyant rise speed (continuous gray line in Figure 9), slightly higher than the

standard case's speed (continuous black line in Figure 9). Both curves are qualitatively similar, but the former has a maximum value of about  $\sim 125 \text{ m s}^{-1}$ , while the later peaks at  $\sim 115 \text{ m s}^{-1}$ , which is a  $\sim 9\%$  deviation. The left-handed flux rope (having the same  $B_0$ ,  $\delta S$ , and  $\Delta\rho/\rho$  as the standard case, dashed black line in the figure) attains a maximum rise velocity of  $\sim 110 \text{ m s}^{-1}$ ,  $\sim 5\%$  less than the standard case. More importantly though, the rise speed profile as a function of height is skewed toward higher radii relative to the standard case. The left-handed flux-rope's speed is initially lower (in the first half of the domain), but it becomes higher afterward. The case with negative polarity (negative  $B_0$ ) follows the standard case very closely and was left out of the plot for simplicity. The cases with weaker  $B_0$  and  $\Delta\rho/\rho$  (red lines in the figure) attain lower buoyant rise speeds, as expected. The weakest of them (dotted red line) does not manage to attain the top of the domain because it is disrupted roughly at mid-height in the CZ. In the first days of the simulation, this flux rope actually acquires a slightly negative speed, hardly managing to counterbalance the convective downflows. This case led us to re-evaluate the threshold for the flux-rope buoyancy. We ran a few extra cases, at different density deficits, to better constrain this threshold. The re-evaluated threshold is represented in Figure 6 with a red dashed line.

Overall, the background magnetic field seems to exert an enhanced drag over the flux ropes. Furthermore, this effective drag depends on the relative orientation of the background and the flux-rope magnetic fields (i.e., on the way the flux rope connects with the external magnetic field).

The bottom panel of Figure 9 further shows that the flux rope traversing a hydrodynamic convection zone evolves smoothly, while the dynamo cases show a more irregular behavior. The amplitude of these variations is small in comparison to the average rise speeds, and it is hardly discernible in the figure. We interpret this feature as the signature of a flux rope opening its way upward by consecutive episodes of reconnection with the background field (cf. Dorc 2007, albeit in a simpler scenario). It is likely that these small deviations to the flux-tube trajectories become larger if higher turbulence levels are attained, as, for example, in Hughes & Falle (1998).

Variations in the initial flux-rope latitude produce a very wide range of buoyant rise speeds, independently of the other flux-rope geometrical parameters. This behavior was already found by Jouve & Brun (2009) both in their convective and isentropic cases with hydrodynamic backgrounds. Similar flux ropes (with the same density deficit, magnetic strength, and twist) will experience different effective buoyancy forces as a function of the background rotation rate, which is non-uniform across the meridional plane (see Figure 1, middle panel). The buoyant force applied to the flux ropes is, per unit mass, proportional to  $g - r \sin^2 \theta \Omega^2(r, \theta)$ . Low-latitude flux ropes cross zones with rotation rates necessarily higher than flux ropes at higher latitudes. This effect is particularly expressive in the cases shown in Figure 9, initially placed at  $15^\circ\text{N}$  and  $45^\circ\text{N}$ . The high-latitude case crosses a region of the CZ with roughly uniform  $\Omega$ , while the low-latitude case crosses layers with increasing  $\Omega$  as it rises through. This makes the difference in flux-rope vertical acceleration actually increase during the buoyant rise, further accentuating the differences. The instantaneous flows each flux rope encounters during the buoyant rise further contributes to increasing its spread in rise speed. In fact, the trajectory of the flux rope placed at  $45^\circ\text{N}$  crosses zones where the background convective flows with  $\langle v_r \rangle_{\phi,t} > 0$ , while

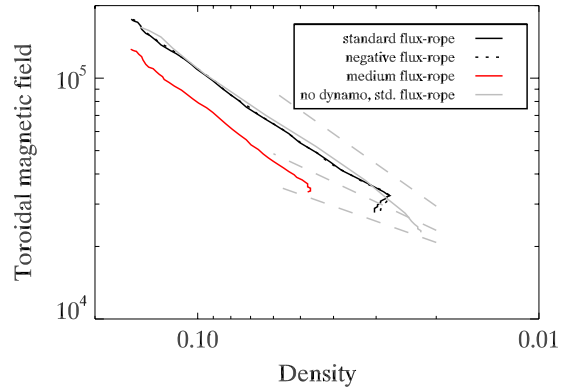


**Figure 10.** Magnetic field strength at the center of the twisted flux ropes  $B_c$  as a function of the total central density  $\rho$  (log-log plot) during the whole runs (buoyant rise, emergence, and later phases). During the buoyant rise, most curves are well fitted by a power law  $B_c \propto \rho_c^\alpha$  with an index  $\alpha \lesssim 1$ ; the exceptions are the weak-field cases, which are severely distorted by the convective flows and lose their spatial coherence. The dashed gray guidelines indicate the slopes for  $\alpha = 1, 2/3, \text{ and } 1/2$ .

(A color version of this figure is available in the online journal.)

its low-latitude counterpart crosses through a more balanced distribution of upflows and downflows both in longitude and in time. This is somewhat specific to the instant chosen to be the initial time  $t_0$  in our model. But, since our simulation had at that instant already achieved a statistically mature state in regards to its convective flows, the flow properties encountered by the flux ropes in our runs are on average representative of any moment.

### 3.3. Flux-rope Expansion, Magnetic Flux, and Density

The magnetic flux ropes expand as they rise buoyantly through the CZ. The flux-rope's magnetic field strength and density are then expected to vary as a result of this expansion. It has been suggested that the evolution of these two quantities is well described by the simple power law

$$B_c \propto \rho_c^\alpha, \quad (22)$$

where  $B_c$  is the flux-rope toroidal magnetic field strength and  $\rho_c$  is the total density inside the flux ropes. Cheung et al. (2010), in particular, have verified that an  $\alpha$ -index between one-half and two-thirds allows for a correct assessment of the combined variations of magnetic field strength and density in their simulations of the later phases of the emergence of a horizontal flux rope. Their study was based on a numerical model that covers a small Cartesian domain spanning roughly  $90 \text{ Mm} \times 50 \text{ Mm}$  horizontally and  $10 \text{ Mm}$  vertically across the photosphere in which a horizontal magnetic flux rope was introduced. We assess now if this result still holds for self-connected toroidal flux ropes, such as those in our setup, and whether it is extensible to the whole of the buoyant rise (from the bottom to the top of the CZ).

Figure 10 shows a log-log plot of the magnetic field strength  $B_c$  as a function of the flux-rope's total density  $\rho_c$  (both measured at the axis of the flux rope) for some of the runs we performed (the legend identifies each of the cases represented). The axis of the flux rope was defined as the position in the poloidal plane where  $|B_\phi|$  is at its maximum. The gray dashed lines indicate the slopes corresponding to  $\alpha = 1/2, 2/3, \text{ and } 1$ . It is readily visible that  $B_c$  scales as  $\rho_c^\alpha$ , with  $\alpha$  only slightly smaller than 1. Each one of the curves in Figure 10 was fitted to the aforementioned power law. We restricted the fitting procedure to the moments

when the flux-rope height is in the interval between  $0.8 R_{\odot}$  and  $0.92 R_{\odot}$  in order to avoid spurious effects due to the proximity of the numerical boundaries. This excludes (for all runs) the initial acceleration at the bottom of the CZ and the braking at the top. The strong-field and more buoyant cases are best fitted with an index  $\alpha = 0.998 \pm 0.001$  (black continuous and dotted lines in Figure 10). The case with a hydrodynamical background (no dynamo) shows a similar behavior, but with a smoother profile and smaller fitting error. These cases are those for which the toroidal symmetry and coherence are better maintained during their whole evolution. Cases with a lower magnetic field strength and lower buoyancy show a slightly steeper power-law index (slightly higher  $\alpha$ ; red curve in Figure 10), but, perhaps more importantly, also show a considerably higher fitting error. Cases with weak fields but strong buoyancy (not represented in Figure 10 for simplicity) remain on average very close to their strong-field counterparts, though with stronger variations. (Their profile is less smooth.) As a side note, we also observed that the evolution of  $\rho_c(r)$  shows very few differences among the different cases, while the dispersion in the  $B_c(r)$  curves is noticeably higher; the evolution of the density at the axis of the flux ropes seems to be defined by the background stratification almost on its own.

Let us now discuss the physical significance of the  $B_c \propto \rho_c^\alpha$  scaling law that we found. We will, for simplicity, consider the magnetic flux tube to be perfectly axisymmetric toroidal structures of circular cross-section. Let us define  $a$  as the minor radius and  $R$  as the major radius of the toroidal tube (the distance between the center of the torus to the center of the tube). The position of the center of the tube is given by  $r$  and  $\theta$ , with the usual meaning in spherical coordinates. The cross-section surface of the tube is  $A = \pi a^2$  and its length is  $L = 2\pi R = 2\pi r \sin\theta$ . The volume of the toroidal flux tube is  $V = A \times L = 2\pi^2 a^2 r \sin\theta$ . The mass and magnetic flux contained in the flux tube are at all times

$$\begin{aligned} M &= \rho A \times L = \rho_c 2\pi^2 a^2 r \sin\theta \\ \Phi &= B_c A = B_c \pi a^2. \end{aligned} \quad (23)$$

These two quantities are conserved during the buoyant rise as long as the mass and magnetic flux exchanges with the environment are negligible, and so the ratio  $\Phi/M$  is

$$\frac{\Phi}{M} L = \frac{B_c}{\rho_c} = \rho_c^{\alpha-1}, \quad (24)$$

with the last equality implying that the power law in Equation (22) holds. Equivalently,

$$\frac{B_c}{\rho_c} \propto L = 2\pi r \sin\theta. \quad (25)$$

That is, both  $B_c$  and  $\rho_c$  depend on the variations in flux-tube cross-section  $a$  (poloidal expansion), but only  $\rho_c$  is sensitive to variations in the tube's length  $L = 2\pi r \sin\theta$  (toroidal expansion). The contribution of the poloidal flux-tube expansion vanishes in Equation (25), as both  $M$  and  $\Phi$  are proportional to  $A = \pi a^2$  (see Equation (23)). If the flux rope varied its cross-section  $a$  while keeping its length  $L$  constant, then the index  $\alpha$  would be exactly equal to 1. Conversely, if the flux rope underwent a purely toroidal expansion (constant  $a$ , growing  $L$ ), then  $0 < \alpha < 1$ . In our simulations, the total flux-rope expansion is a combination of both the toroidal and poloidal components. The torus length  $L \propto r$  increases during the buoyant rise, and

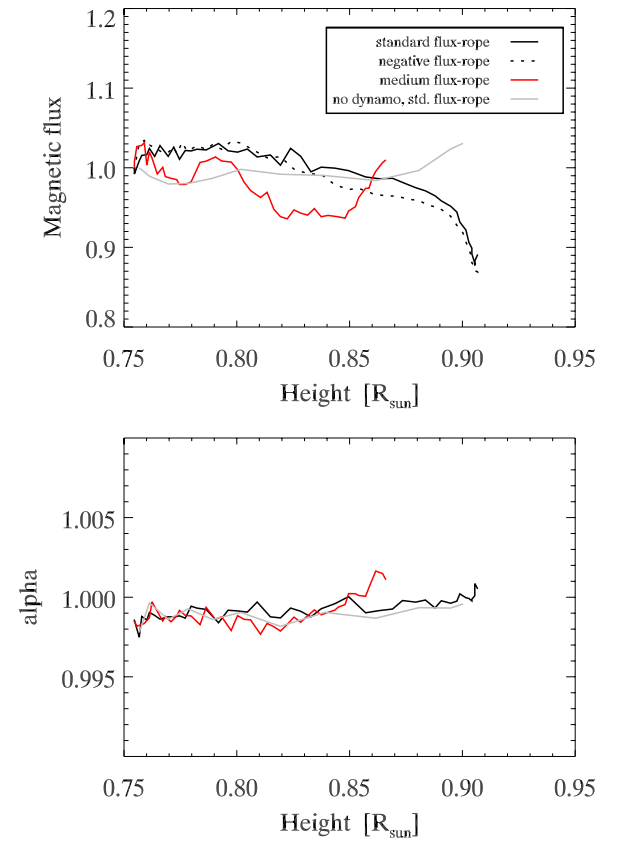


**Figure 11.** Top panel: relative variation of the magnetic flux contained in the twisted flux ropes as a function of the position of the flux-rope's axis. Bottom panel: index  $\alpha$  as obtained from Equation (24), using the ratio of magnetic flux to mass in the buoyant flux ropes.

(A color version of this figure is available in the online journal.)

so does the flux-rope's cross-section (due to the background pressure radial profile). As stated above,  $\alpha \lesssim 1$  in all our runs, meaning the poloidal component of the flux-rope expansion dominates over the toroidal component.

Of course, these arguments rely on the assumption of conservation of mass and magnetic flux inside the buoyant flux rope (and more specifically, on the conservation of the ratio  $\Phi/M$ ). We need to verify if this assumption fails, or at least how much the leakage of mass and magnetic flux affects the results. As stated before (Section 3.1), a fraction of the peripheral magnetic flux is continuously dragged within the wake, which forms behind the flux rope as it rises buoyantly. It is also likely that reconnection occurring around the flux ropes and any other diffusive process altogether lead to a flux exchange with the surroundings. The top panel in Figure 11 shows the evolution of the magnetic flux  $\Phi$  contained within the twisted flux ropes as a function of height, as the ropes rise through the CZ. The curves indicate that the losses (to the surroundings) are substantial, especially in the later phases of the buoyant rise. The stronger inflection of the black continuous and dotted lines in the upper part of the domain is due to the flux-emergence episode; the curves represent the interval  $t = 0$  to  $t \sim 15$  days, with the emergence episode starting roughly at  $t = 12$  days. Weaker-field flux ropes suffer stronger losses, and the flux rope evolving in a hydrodynamic background better verifies flux conservation. The evolution of the mass contained in the flux ropes correlates very well with that of the magnetic flux (i.e., magnetic flux exchange is dominated by processes also implying

mass exchange). The bottom panel in Figure 11 summarizes the combined effect of the variations of  $\Phi$  and  $M$  on  $\alpha$ . The index  $\alpha$  is obtained by re-arranging Equation (24) as

$$\alpha = \frac{\log(\Phi L/M)}{\log \rho_c} + 1. \quad (26)$$

This confirms the  $\alpha \lesssim 1$  value found above. This result holds for all cases studied, including for different flux-rope buoyancy forces and initial latitudes.

### 3.4. Magnetic Energy Balance

The evolution of the total ME is described by the equation

$$\frac{d}{dt} \int_V \frac{B^2}{8\pi} dV = - \int_V \frac{J^2}{\sigma} dV - \frac{1}{c} \int_V (\mathbf{J} \times \mathbf{B}) \cdot \mathbf{v} dV - \oint_S \mathcal{S} dS, \quad (27)$$

where the terms on the right-hand side represent, respectively, the ohmic diffusion rate, the rate of work done by the Lorentz force, and the energy loss rate transported by the Poynting flux across the domain's top and bottom boundaries. The ohmic diffusion term is always an energy sink, while the other two terms on the right-hand side of Equation (27) can act as either energy sources or sinks. The magnetic work rate term  $-\frac{1}{c} \int_V (\mathbf{J} \times \mathbf{B}) \cdot \mathbf{v} dV$  is, for example, positive when magnetic structures induce flows in the system and negative when the flows shear the magnetic structures with little or no feedback on the former. The Poynting vector (in the Poynting flux term) is defined as

$$\mathcal{S} = \frac{c}{4\pi} \mathbf{E} \times \mathbf{B}, \quad (28)$$

with  $\mathbf{E}$  being the electric field vector, and quantifies the electromagnetic energy transfer rate across a surface, which is, in other words, the total electromagnetic energy that leaks into or out of the system. Considering a finite conductivity  $\sigma = c^2/(4\pi\eta)$  and Ohm's law  $\mathbf{J}/\sigma = \mathbf{E} + \mathbf{v} \times \mathbf{B}$ , this vector becomes

$$\mathcal{S} = \frac{\eta}{c} \mathbf{J} \times \mathbf{B} + \frac{c}{4\pi} [B^2 \mathbf{v} - (\mathbf{v} \cdot \mathbf{B}) \mathbf{B}]. \quad (29)$$

The second and third terms in the right-hand side of Equation (29) describe, respectively, the advective transport of the ME density and the propagative energy transport supported by the magnetic tension (e.g., Alfvén waves excited by transverse motions). The first term on the right-hand side is most often neglected in ideal MHD studies, and we always observe it to be much smaller than the other terms in our simulations in spite of the finite diffusivity. The radial component of this vector (i.e., the component orthogonal to our domain's boundaries) is, in CGS units,

$$\begin{aligned} \mathcal{S}_r = & \frac{\eta}{c} [J_\theta B_\phi - J_\phi B_\theta] \\ & + \frac{c}{4\pi} [v_r (B_\phi^2 + B_\theta^2) - B_r (v_\phi B_\phi + v_\theta B_\theta)]. \end{aligned} \quad (30)$$

Analyzing the Poynting fluxes obtained from numerical simulations requires some special precautions. These are most often computed at the numerical boundaries of the computational domains, and therefore the specific choice of boundary conditions certainly influences the Poynting flux amplitudes. Equation (30) separates the effects of the conditions imposed on components of the velocity parallel and those perpendicular to the boundary (in our setup  $v_\theta$  and  $v_\phi$  are parallel, while  $v_r$  is perpendicular). It

also shows how the Poynting flux strongly depends on the parallel components of the magnetic field; for example, matching the boundary magnetic field to an external radial field imposes a null Poynting flux there (cf. Brun et al. 2004). In our setup, the magnetic field is matched to an external potential field, thus allowing for ME leakage through the boundaries. The parallel components of the velocity are also allowed to vary in time at the boundaries. The advective component of the Poynting flux is neglected (due to the boundary condition imposed for  $v_r$ ), but this term is probably smaller in comparison to the third term on the right-hand side of Equation (30) at the top of the CZ in the real Sun. We tested the consistency of the ME balance in our models in two ways. First, we computed the radial Poynting fluxes at all points (in the radius) of our model's domain and verified that there were no noticeable boundary layer effects. Second, we directly compared the left-hand side and the right-hand side of Equation (27) and verified that the equality holds with numerical precision at all times, meaning that leakage and diffusion are consistently accounted for in the simulations.

Figure 12 shows the temporal evolution of the total ME (top-left panel), together with its source/sink terms, for some of the runs in Table 2 during a time interval of up to 60 days after the introduction of the magnetic flux ropes. The background dynamo run (with no flux rope introduced) is superimposed for comparison. The flux ropes introduced in the system correspond to very strong concentrations of magnetic field, and so the total ME is much higher than that of the background dynamo at the moment of introduction ( $t = 0$  in Figure 12, top left panel). This is true even for the weaker magnetic cases we ran (red and blue lines). This initial perturbation in the ME is, of course, a consequence of our method and it would not take place if such flux ropes were generated self-consistently by the magnetoconvective flows in the CZ, as is the case in Nelson et al. (2011, 2013) for fast rotating solar-like stars. However, this issue is beyond the scope of this paper and requires future investigation.

The ME decays quickly during the buoyant rise of the flux ropes (the first 12 days for the standard flux rope). During this phase, the energy losses are initially dominated by the ohmic diffusion (top right panel), but the work done by the Lorentz force grows as the flux rope gains momentum due to the buoyant force. Let us explain this effect. The bottom left panel shows that the magnetic work term is indeed negative during the whole buoyant rise phase for all cases represented, peaking at about the moment when the buoyant rise speed is maximal. That happens because the rising flux rope induces a flow around itself in the CZ, as shown in Section 3.1. This translates into work done by the Lorentz force, which transforms ME into KE. Note that the sign of this term changes afterward, as the buoyant rise ends. In the later phases, well after the flux-emergence episode (which happens at about  $t = 12$  days for the standard case), the ME curve inflects and starts varying almost in parallel with the unperturbed dynamo case. At this point, the dynamo processes have taken over the perturbations forced by the buoyant flux ropes in the background flows, and the magnetic work term is consistently positive.

The bottom-right panel of Figure 12 shows the total Poynting flux  $\mathcal{S} = \mathcal{S}_{\text{top}} - \mathcal{S}_{\text{bottom}}$ . The initial spike visible in all the Poynting flux curves corresponds to the contribution of the flux crossing the lower boundary of the domain  $\mathcal{S}_{\text{bottom}}$ , which is only important in the beginning of the simulations (during the first 4 days) and has a positive contribution to the system's ME. The Poynting flux curves peak again during the

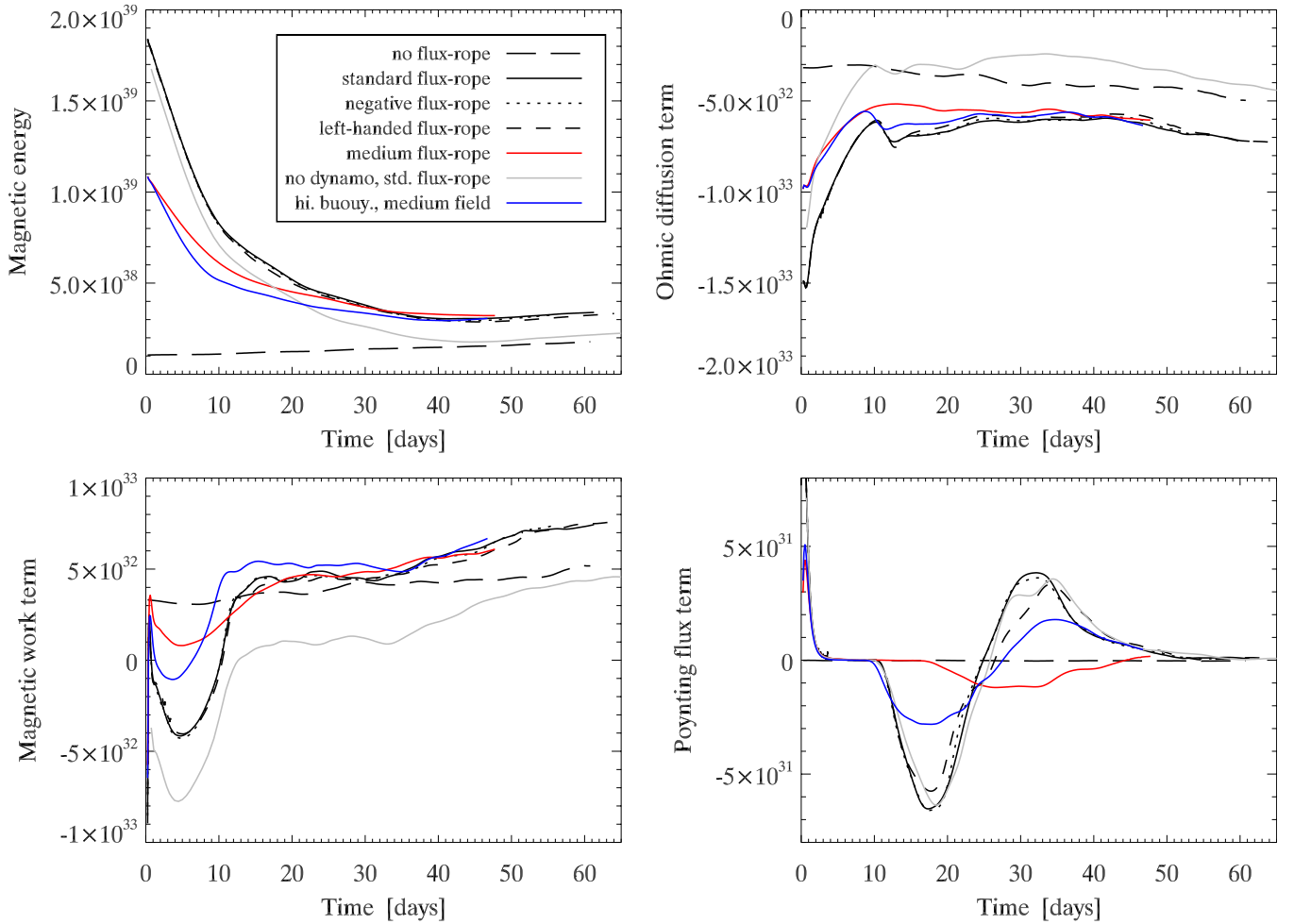


**Figure 12.** Evolution of the total magnetic energy in the whole numerical domain for different cases presented here (standard case, medium  $B$ -field cases, and standard case in a hydrodynamical convection zone). The first panel (top, left) shows the total magnetic energy as a function of time, while the other panels show the source/sink terms in the equation for  $\partial_t \int B/8\pi dV$ , namely the rates of ohmic diffusion, the rate of work done by the Lorentz force, and the Poynting flux. The abscissas represent time in days with  $t = 0$  at the moment when the flux rope is also shown (long dashed line).

(A color version of this figure is available in the online journal.)

flux-emergence episode ( $t = 10$ – $22$  days for the standard case) and this time are dominated by the flux crossing the upper boundary  $S_{\text{top}}$ . This peak has a negative sign, meaning ME is being transferred outward to the corona. The amplitude of the Poynting flux depends both on the flux-rope magnetic field strength and buoyant rise speed. This is understandable in view of Equations (29) and (30) and the fact that the amplitude of the surface flows induced by the flux-rope rise and emergence depends directly on the buoyant rise speed.

The black and blue lines in the plot correspond to flux ropes with the same buoyancy but different  $B_0$ ; the former have a stronger magnetic field (standard case) than the latter. The weaker flux rope produces a Poynting flux that is smaller than the standard case by a factor of two, even if the initial  $B_0$  is only smaller by a factor of 1.25, which is consistent with  $S \propto B^2$  (the surface flow velocities being the same). Note that the match is not perfect; we are comparing initial state parameters with later diagnostics, and each of the flux ropes suffer from different environmental effects in their evolution from the bottom to the top of the CZ. The blue and red lines correspond to cases with the same initial magnetic field strength, but with the former being more buoyant than the latter. Both the time delay of about

10 days and the difference in amplitude relate directly to the different buoyant rise speeds across the CZ.

The total ME evolution depends weakly on the flux-rope’s polarity and handedness, even though these properties lead to important differences in the surface signatures of flux emergence (as we will see later on). The flux-rope’s magnetic field does interact with the surrounding dynamo field; differences in amplitude, polarity, and handedness induce changes in the evolution of the flux ropes themselves but translate into a small effect in the evolution of the ME of the whole system.

Figure 12 also shows a few other interesting points. The ME in the case with a purely hydrodynamical convective background decays faster than all the others, as in the latter the energy decay due to the flux-rope rise and expansion accounts for only a fraction of the total ME. But, later in its evolution (for  $t \geq 40$  days), the ME starts growing at a temporal rate close to that of the dynamo run. At this stage, the flux rope is already well past the emergence episode and the associated magnetic fields have already been strongly disrupted by the shearing flows at the upper layers of the CZ (see Section 5.1). The flux-rope’s magnetic flux that did not emerge is now seeding a (local) dynamo.

The cases where weaker magnetic flux ropes were added to the dynamo background show a somewhat surprising behavior. Their associated ME decays more slowly than that in the strong field cases, even if they are less robust in the face of disruption by the background convective flows (smaller magnetic stresses to counterbalance deformations imposed by the flows) and the dynamo field (reconnection events should take away a higher fraction of the flux-rope’s own field). The most important parameter here seems to be the buoyant rise speed. Lower rising speeds mean that cross-section  $A$  of the flux ropes will expand more slowly in time (as the flux ropes take longer to attain the less dense layers of the CZ), and therefore, the nominal magnetic field  $B_0$  will also decrease more slowly (because  $B \propto A^{-1}$ , the total magnetic flux in the flux ropes being approximately conserved). The flux-rope’s contribution to the total magnetic field scales as  $B_0^2$ , so this effect becomes important. Note how flux ropes with the same initial magnetic field strengths but different buoyancy forces assume different decay rates (the red/blue pairs of lines, with the blue representing cases with the same magnetic field strength but higher buoyancy).

The buoyant rise speeds for each case can be inferred from the  $\Delta\rho/\rho$  values in the diagram in Figure 6 and verified in Figure 9. The blue and red lines bifurcate in Figure 12, such that the blue lines (more strongly buoyant) start decaying faster—at a rate close to that of the “strong-field” cases, which have the same initial  $\Delta\rho/\rho$  (black lines in the plot).

#### 4. POST-BUOYANT RISE PHASES

In this section, we focus on the manifestations of the arrival of the buoyant magnetic flux ropes at the top of the domain after they crossed the convection zone. For simplicity, we will hereafter use the term “surface” to refer to the top of the numerical domain and define flux emergence as strong and localized enhancements of the magnetic field at the top of the domain caused by the arrival of rising flux ropes. We also define a magnetic flux-emergence episode as the time interval from the first signs of flux-rope-related variation of the magnetic flux crossing the surface up to the peak in surface magnetic flux and energy. These moments correspond, respectively, to  $t = 10$  days and  $t = 22$  days for the standard case in our simulations (note that these timings could be different in real solar events).

##### 4.1. Emergence Precursors

We will focus here on identifying features that consistently precede the actual flux-emergence episode in our simulations. Figure 13 shows the temporal evolution of the radial velocity  $v_r$ , the unsigned magnetic field  $|B_r|$ , the current density squared  $J^2$ , and the magnetic helicity  $\mathbf{A} \cdot \mathbf{B}$  evaluated at the surface and within the latitudinal interval where flux emergence occurs as a function of time. The earliest tracer of flux-rope rise and emergence is the radial velocity  $v_r$ , which also correlates well in time with the surface density fluctuations  $\rho$ . The latter has a very weak signal though and is not represented in Figure 13 for simplicity. These tracers gradually increase during the whole flux-rope buoyant rise and peak at the moment when the flux-emergence episode starts (that is, when the surface magnetic flux and energy start increasing). This occurs about 12 days before magnetic flux and energy due to the flux-rope emergence reach their maximum value in the standard case. The same time delay is observed for the cases with weaker flux-rope magnetic fields but the same buoyancy. The  $v_r$  signal has the same amplitude as the standard case but the surface magnetic fields naturally

peaks at a lower value. Lower buoyancy flux ropes generate much weaker  $v_r$  signals; the red line in the top left panel in the figure represents a flux rope with an initial  $B_0$  that is 0.75 times that of the standard case (black continuous line). The magnetic field signal keeps an amplitude close to that of all other flux ropes with the same initial  $B_0$  but different buoyancies. The delay between  $v_r$  and  $|B_r|$  is higher in this case—on the order of 15 days. The surface  $v_r$  (and also  $\rho$ , albeit with a very weak signal) are, therefore, observable precursors to the formation of solar active zones. The physical cause for this behavior lies on the dipolar flow self-consistently generated by the flux rope itself as it rises through the CZ (see Section 3 and Figures 7 and 8). Namely, the radial upflow that forms above the flux rope extends radially up to the surface. A transient overdense patch forms there as the upflow is stronger closer to the flux rope than farther away from it, meaning plasma accumulates just below the surface increasingly faster than it manages to be evacuated horizontally. This phenomenon ends as soon as the flux rope starts slowing down at the upper part of the CZ (the buoyancy is reduced there). The amplitude of the surface  $v_r$  and  $\rho$  signals is directly related to the flux-rope’s buoyant rise speed (that is, to  $\Delta\rho/\rho$ ), with more buoyant flux ropes producing stronger signals.

An additional interesting feature is the temporal evolution of  $J^2$ , as it starts growing roughly at the same time as the other magnetic quantities (that is, when the flux-emergence episode starts) but then grows much faster. Its peak value occurs at about 2 days after  $v_r$  and  $\rho$  peak, and 10 days before the magnetic flux and energy do in the standard case. These time delays are similar in the case with a hydrodynamical background (gray line in the plots). Also, the amplitudes of the  $J^2$  signals are naturally stronger for the cases with stronger field flux ropes. In fact,  $J^2$  is a good tracer of the boundary of the flux rope, as that is where the magnetic gradients are the strongest. The time lags (of  $\sim 10$  days in the standard case) between the peaks of  $J^2$  and  $|B_r|$  are consistent with the flux-rope rising speeds and the physical distance between its axis and its periphery. The magnetic helicity  $\mathbf{A} \cdot \mathbf{B}$  signal, contrary to the previous diagnostics, also depends on the handedness of the emerging flux rope. Right-handed and left-handed flux ropes produce quasi-symmetric signatures during the emergence episode. In the post-emergence phases, this symmetry is broken though, as both the left- and right-handed magnetic flux ropes are sheared in the same direction by the convective surface flows. The last panel in Figure 13 clearly shows the initially symmetric evolution for the right- and left-handed flux ropes ( $t = 10$ –12 days) and the inflexion happening thereafter. The two lower panels in Figure 13 also show the magnetic field amplitude and helicity for the high- and low-latitude cases, as they exhibit remarkably different behaviors. The high-latitude case produces a perturbation in  $|B_r|$  similar to that of the standard case, while the low-latitude case shows a weaker and more delayed perturbation. The low-latitude flux rope effectively rises more slowly (see Figure 9) and is distorted to a greater extent by the convective flows. The magnetic helicity evolution perturbations have initially opposite signs, even though both the flux ropes (high and low latitude) have the same polarity and handedness. The difference lies in the specific surface shearing motions (the differential rotation) encountered at the latitude of emergence.

The results presented in this section offer a viewpoint complementary to that proposed by local helioseismology studies (Ilonidis et al. 2011; Kosovichev 2012; Hanasoge et al. 2012), which have been producing increasingly more detailed

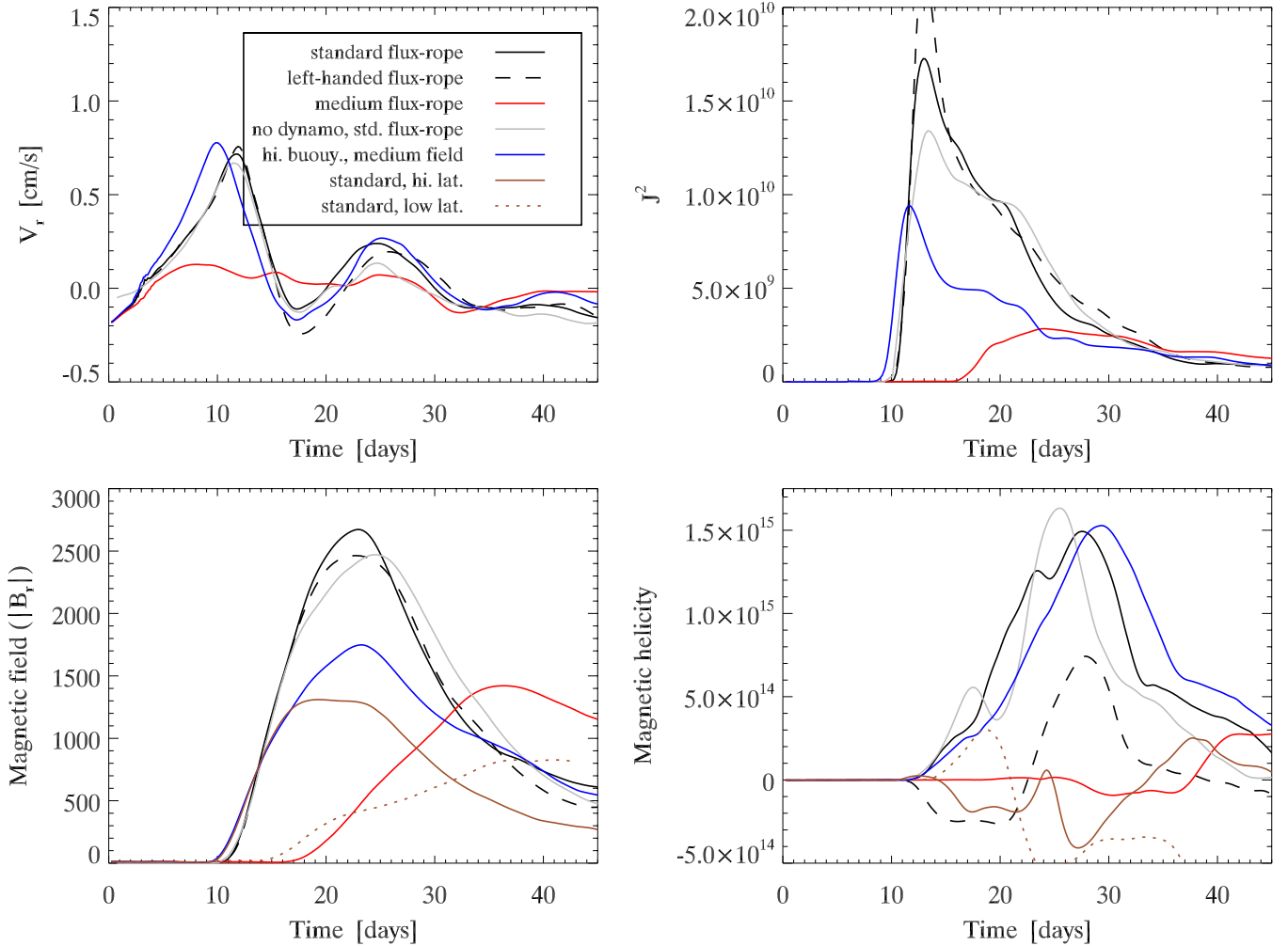


**Figure 13.** Surface variations (relative to the background state) of the radial velocity, unsigned magnetic field strength, current density squared, and magnetic helicity before and during the flux-emergence episode averaged over the latitude interval where magnetic flux emerges. Note how the maximum of the quantities  $v_r$  and  $J^2$  precede that of the other ones. The amplitude of the  $v_r$  signal is mostly determined by the flux-rope’s rise speed. There is also a signal in surface density (not shown here) that correlates very well with  $v_r$  but has a small amplitude. Surface magnetic field strength and current density are determined by the flux-rope’s strength; the magnetic helicity further depends on the handedness of the emerging rope.

(A color version of this figure is available in the online journal.)

constraints about the sub-surface flows in the first few megameters below the solar surface and about the possible early detection of rising flux ropes. As such, these new methods may provide in the near future the means to verify our findings. The upper boundary of our numerical domain lies just below, at  $r = 0.97 R_\odot$ . Furthermore, the quantitative details of the temporal profiles in Figure 13 are probably influenced by the boundary conditions imposed there. Despite these reasons, we believe that the qualitative properties of the results discussed in this section may be generalized, to some extent, to the solar surface. Note that here we do not aim to produce reliable quantitative predictions of such surface flux-emergence precursors. This problem is currently being addressed using models whose numerical boundary lies above the photosphere and that account for the radiative losses taking place there (see Pinto & Brun 2011). Preliminary results suggest that the qualitative properties of the flux-emergence precursors described here are correct (in the sense that they are not a direct consequence of the domain truncation and upper-boundary conditions). Please note that while the exact time delays and amplitudes we found may not transpose directly to the Sun, the temporal ordering between the different diagnostics should remain the same.

#### 4.2. Surface Fields

We now turn our attention to understanding how the surface magnetic field and flows react to the emergence of a twisted magnetic flux rope. Figure 14 shows three time series of synthetic magnetograms (that is, surface maps of  $B_r$ ) for the standard case (top row), the case with a flux rope with negative  $B_0$  (second row), and the case with a left-handed flux rope (third row). The instants represented are, from left to right,  $t = 12, 15, 25,$  and  $45$  days. The panels only show a sub-domain of the magnetic active lane generated by the emergence of the flux ropes.

The flux ropes were initially placed near the bottom of the CZ at  $30^\circ\text{N}$  and then rose almost radially, deflecting northward by a small amount. The activity lane then first appears at the surface between latitudes  $30^\circ\text{N}$  and  $40^\circ\text{N}$ . The slow poleward drift continues after the flux rope reaches the surface and stops buoyantly rising. The flux rope is then advected by the sub-surface poleward meridional circulation (see Section 3 and Figures 7 and 8, in particular the CCW circulation crossing the flux rope in the last panel). About 10–15 days after the beginning of the emergence episode, the active lane occupies the latitudinal

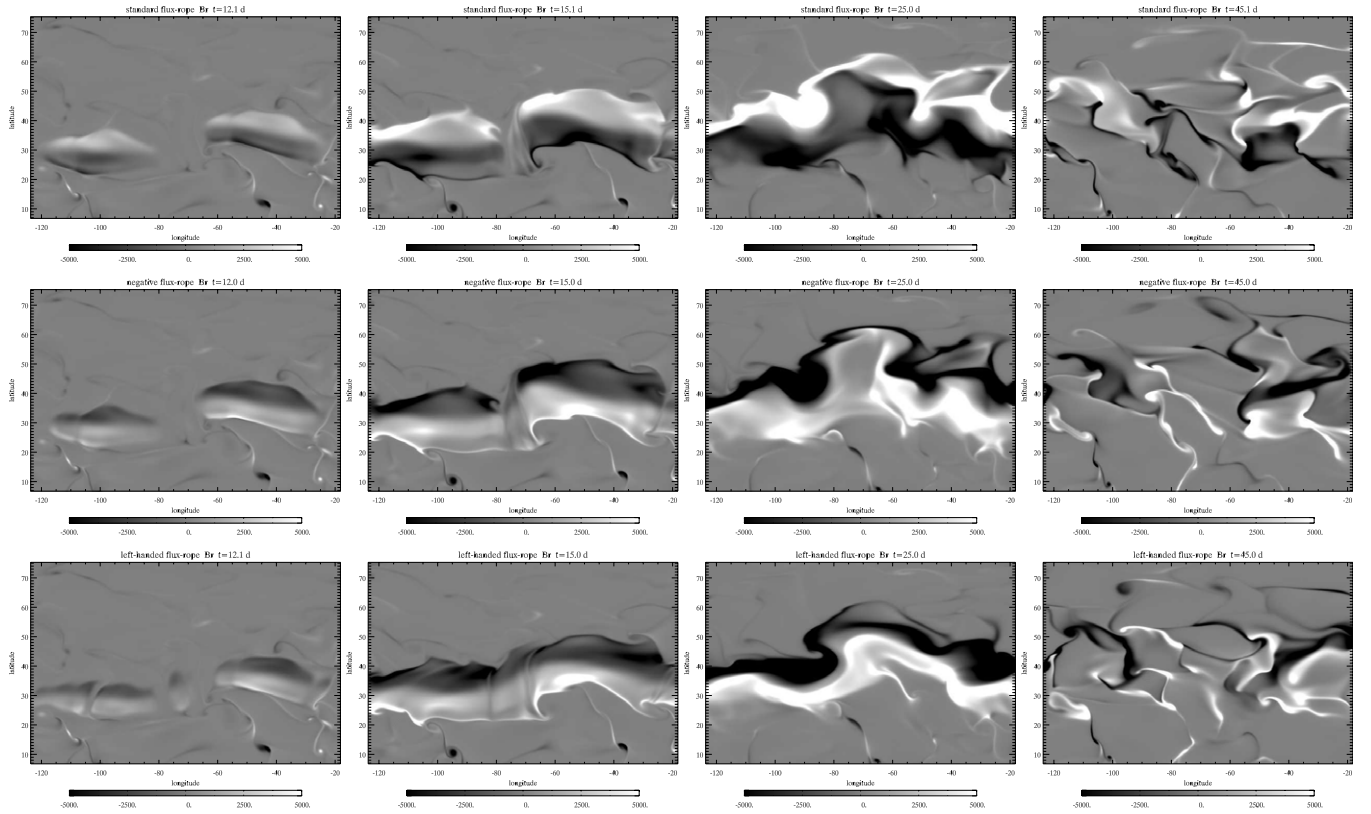


**Figure 14.** Close-up view of the surface radial magnetic field  $B_r$  during the flux-emergence episode at different instants (from left to right,  $t = 12, 15, 25,$  and  $45$  days). The first row represents the standard case; the second row represents the negative polarity case; and the third row represents the left-handed case. The color scale is saturated at  $\pm 5$  kG.

interval  $40^\circ\text{N}$  to  $50^\circ\text{N}$ . Besides the poleward drift, the active lane also broadens in latitude as the rope's emerged magnetic flux is sheared and advected by the convective flows, and undergoes resistive diffusion.

The flux-emergence episode starts with a series of discontinuous patches of magnetic field appearing at the surface ( $t = 12$  days, first column in Figure 14), even though the flux ropes are initially perfectly axisymmetric. This is due to the influence of the convective motions encountered by the flux ropes during their buoyant rise. The fractions of the flux rope that cross strong downflow plumes are delayed relative to the rest, while those encountering rising convective blobs are pushed forward. The maximum delay between the first and the last emerging parts is about 5 days. The distortion will be more accentuated for flux ropes with weaker magnetic field strength. The least buoyant ropes in our set of simulations do not fully emerge, as some sections do not manage to overcome the local convective downflows they encounter. A few days after the beginning of the flux-emergence episode, the bulk of the flux rope has stopped its buoyant rise, and a larger fraction of its magnetic flux has reached or crossed the surface, making the azimuthal non-uniformities stated above fade away (second column in Figure 14,  $t = 15$  days). The orientation of the magnetic polarity is mainly north–south at this moment. In other words, the polarity inversion line (PIL) is essentially aligned with the  $\phi$  direction, and there is a well defined and uniform tilt angle of  $\pm 90^\circ$  (the sign depending on the flux-rope's polarity and/or handedness). The surface magnetic flux continues growing until  $t = 23$  days (cf. bottom left panel in Figure 13). During this last phase of the flux-rope emergence, the magnetograms seem to indicate that the emergence regions are rotating. This effect

is particularly noticeable in the northern and southern edges of the emerged structure. Furthermore, the sense of rotation depends on the handedness of the flux rope; right-handed flux ropes exhibit a CCW rotation while left-handed flux ropes turn CW. The rotation patterns do not match the surface flows' velocities. The observed rotation patterns are only apparent and a signature of the flux-rope's own magnetic field as it crosses the surface. For this reason, the flux-rope's handedness determines the sense of the apparent rotation of the emerging magnetic field.

As the simulation proceeds, the surface convection gradually overcomes the perturbation introduced by the flux-rope emergence. The emerged upper fraction of the flux rope is gradually twisted by CCW-rotating vortices. The PIL gets sheared accordingly, but it keeps a global continuous structure for a long period of time (third column in Figure 14,  $t = 25$  days). At about  $t = 30$ – $40$  days, all traces of the emerged flux rope start to disappear. At  $t = 45$  days, all the flux-rope's emerged magnetic flux has been pushed into the network between the convection cells (fourth column in Figure 14). As discussed in Section 3.4, the flux-rope's remaining magnetic field (i.e., the part that has not emerged) has now been assimilated by the solar dynamo.

The emergence of a magnetic flux rope is preceded by a local increase in radial velocity and current density, as described in Section 4.1. In the first two rows of Figure 15, one can see the temporal evolution of the radial velocity  $v_r$  and the current density squared  $J^2$  for the standard case (compare with first row of Figure 14). The current density squared is displayed in a log-scale plot to make its spatial distribution more visible, as the contrast between the background current density and that of the emerging region can be very large. The instants represented

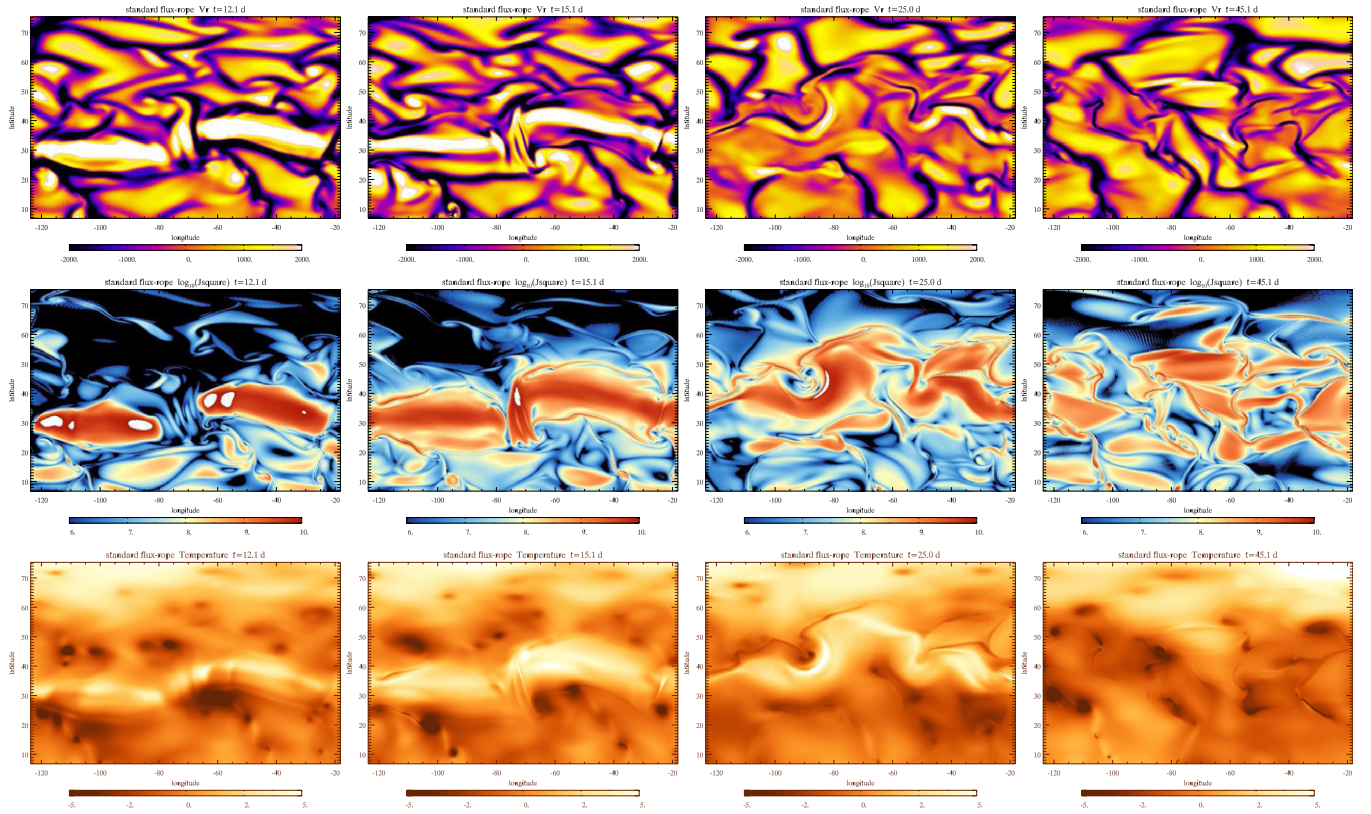


**Figure 15.** Close-up view of the radial velocity  $v_r$  (first row), the square of the current density  $\log(J^2)$  (second row, in a log-scale plot to make its spatial distribution more visible), and the temperature fluctuations  $T$  (third row) for the standard case. The sub-domain and instants represented are the same as in Figure 14.

(A color version of this figure is available in the online journal.)

are the same as in Figure 14: from left to right,  $t = 12, 15, 25,$  and  $25$  days. The surface sub-domain represented is also the same.

The delays between the maximum of  $v_r$ ,  $J^2$ , and  $\|B_r\|$  are quite visible in the figure. The first two peak near  $t = 12$  days (first column), while the last only peaks at  $t = 23$  days (that is, close to the instant represented on the third column). It is interesting to note how the amplitude of the  $v_r$  signal fades away quickly but some traces of it remain until later on. The current density at the surface evolves with a spatial and temporal pattern close to that of  $\|B_r\|$ , but its amplitude is at its maximum earlier in the flux-emergence episode. The temperature fluctuations  $T$  (relative to  $\bar{T}$ ) for the standard case are also represented in the third row. Hot spots (or bands) appear all along the emerging region. Its spatial distribution correlates well with  $v_r$ ; the hotter zones correspond to the strongest upflows, while the cold spots correspond to the top of the convective downflow plumes that form at the intersection of the convective cell boundaries. The contribution of the current density (or rather the ohmic diffusion  $\eta J^2$ ) does not suffice to explain the temperature variations found.

The case with a flux rope placed at a higher latitude shows behavior very similar to that of the standard case. In the low-latitude case, on the other hand, the emerged field organizes into a much more discontinuous pattern, and the emergence episode lasts longer (almost 20 days). This is a consequence of the flux-rope’s slower buoyant rise and of it being more distorted by convective flows during that period. The total emerged magnetic flux is, nevertheless, equally high (mostly due to the larger circumference of a low-latitude flux rope).

### 4.3. Induced Zonal Flows and Surface Shear

The rise of the magnetic flux rope also perturbs the global background state by inducing a zonal (azimuthal) flow inside the flux rope itself. Initially, the rotation rate of the flux rope perfectly matches the background rotation state. The flux rope then rises as a coherent and self-connected magnetic structure. The plasma inside the flux rope thus needs to decrease its azimuthal velocity with respect to the background in order to conserve angular momentum. Figure 16 shows a conical cut taken at  $30^\circ\text{N}$  latitude (a  $\{r, \phi\}$  map for a given constant  $\theta$ ). The color scale represents the azimuthal velocity  $v_\phi$  (relative to the rotating frame, with  $\Omega = \Omega_0$ ; see Section 2.1) at an intermediate phase of the flux-rope trajectory. Contours of  $B_\phi$  are superimposed to trace the position of the flux rope. Note that the relative amplitude of these “backward” flows is high ( $200 \text{ m s}^{-1}$  in the figure, but becoming as high as  $300 \text{ m s}^{-1}$  in some cases) and that they remain strong when the flux ropes reach the surface. At the surface, the  $v_\phi$  signal shows an initial sharp increase, reaching its peak surface value in  $\sim 1$  day after the emergence episode starts, and then fades away more smoothly (the signal disappears in  $\sim 5$  days). Figure 17 shows surface maps of  $v_\phi$  similar to those in Figure 14. It is clear from this figure how a strong azimuthal shear is imposed at the surface during the flux-emergence episode. This strong shearing is nevertheless transient. Its amplitude decays and fades away quickly; the signal is almost indiscernible 5 days after the beginning of the emergence episode. Also, the surface  $v_\phi$  perturbation is centered around the PIL, as it is carried upward within the emerging flux rope. The latitudinal width of the

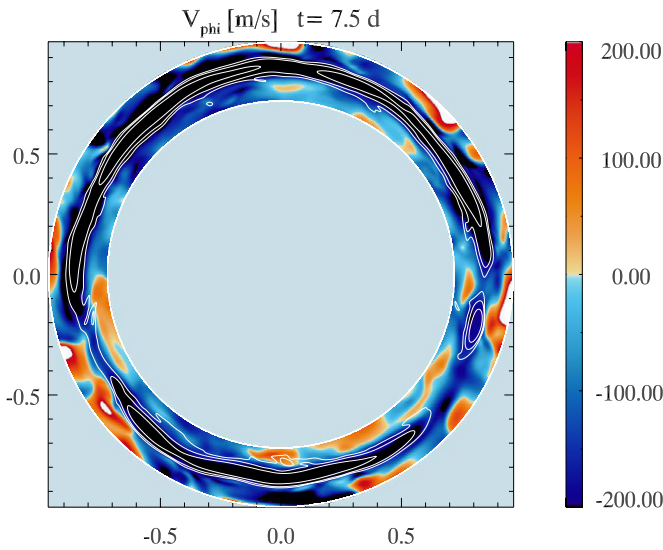


**Figure 16.** Zonal (azimuthal) flow generated inside the flux rope at  $t = 7.5$  days for the standard case. The figure shows a conical slice taken at the latitude of introduction of the flux rope. The color scale represents the azimuthal velocity  $V_\phi$  (between  $\pm 200 \text{ m s}^{-1}$ ) in the rotation reference frame. The white lines are contours of  $B_\phi$ .

(A color version of this figure is available in the online journal.)

perturbation is close to that of  $B_r$  and  $v_r$  in Figures 14 and 15. The maximum surface shearing amplitude ( $\propto \partial_\theta v_\phi$ ) caused by the zonal flow therefore takes place near the boundaries of the emerging flux rope.

We note that the retrograde zonal flows inside the flux ropes are always predominantly azimuthal, showing little toroidal vorticity. The magnetic field inside the flux rope remains twisted and rotates azimuthally as a whole, rather than enforcing a noticeable inner helical zonal flow.

Figure 18 shows the evolution of these retrograde zonal flows for different runs. For the strong  $B_0$  cases, the one evolving in a hydrodynamical background develops the strongest zonal flow. The positive polarity cases in a dynamo background then follow, and the negative polarity case produces the weakest zonal flow. Comparison with Figure 18 shows that the flux ropes attaining a higher buoyant rise velocity also produce stronger retrograde flows. Despite its variations during the buoyant rise, the amplitude of the induced zonal flow always seems to converge to the same surface value right after the flux-emergence episode, at least for the same flux-rope's buoyancy (same  $\Delta\rho/\rho$ ). We also note that the later (post-emergence) evolution seems to depend strongly on the flux-rope's polarity (cf. Section 5.1).

We now test whether angular momentum conservation can be the sole (or the dominant) cause for the zonal flow generation. If this is the case, the amplitude of the retrograde flow must only depend on position, and not on the actual buoyant rise velocity, for any given run. The middle panel in Figure 18 shows the zonal velocity amplitude as a function of radius. It is clear how all runs follow a very close path in this plot, at least in the first half of the convection zone. The flux ropes break down in a sub-surface of small radial extent in the upper part of the convection zone. Some of the runs show a clear departure from the main track in this breaking region. This is especially true for the run with a negative magnetic polarity flux rope, meaning the other physical processes involved have to be related to the magnetic topology and the way the flux rope connects with the dynamo field. The bottom panel in Figure 18 more precisely shows that the retrograde zonal flow amplitudes inside the flux ropes are

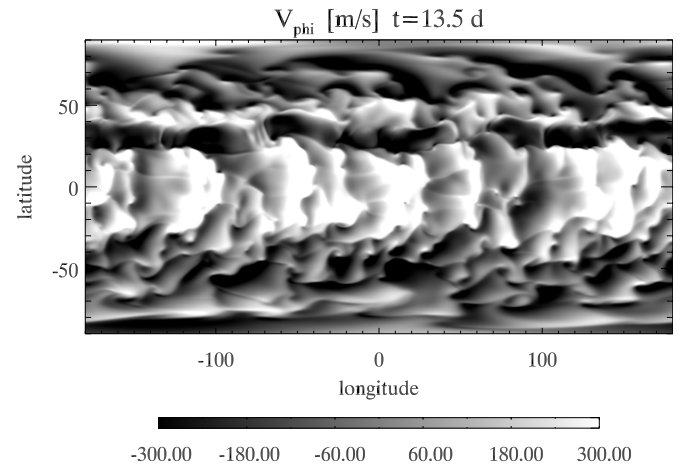


**Figure 17.** Azimuthal surface flows at  $t = 13.5$  days due to the zonal flow generated inside the flux rope during the buoyant rise in the standard case. The color scale is saturated at  $\pm 300 \text{ m s}^{-1}$ .

mostly a consequence of angular momentum conservation. We define the cylindrical radius

$$R = r \sin \theta \quad (31)$$

as the distance of a point to the rotation axis of the Sun. The azimuthal velocity in the inertial reference frame is

$$v_\phi^{\text{inertial}} = v_\phi + \Omega_0 R. \quad (32)$$

Conservation of angular momentum then implies simply

$$v_\phi^{\text{inertial}} \propto R^{-1}. \quad (33)$$

The bottom panel in Figure 18 shows  $v_\phi^{\text{inertial}}$  as a function of the cylindrical radius  $R$  in a log-log plot for all runs. The dotted gray line is a guideline indicating the slope of an  $R^{-1}$  curve. The sections of the plotted lines parallel to this guideline therefore correspond to parts of the flux-rope's trajectories where the angular momentum inside them is strictly conserved. We note that this holds for most of the buoyant rise, at least until the flux rope starts braking near the top of the convection zone and angular momentum is necessarily exchanged with the external medium. This moment corresponds to the flux-emergence episodes discussed previously and to the inflexion point present for all the curves plotted in the bottom panel Figure 18. Past this episode, the flux rope still maintains its spatial coherence for some time and starts being advected poleward by the sub-surface meridional flow (hence the decrease in cylindrical radius, but not in height). This phase corresponds to the upper branch (past the inflexion point) in the same plot. It is interesting to note that the zonal flow inside the flux ropes remains close to angular momentum conservation in these later phases. The departure to a conservative path is carried out mostly by intermittent exchanges of momentum, plasma, and magnetic flux with the environment.

## 5. GLOBAL MAGNETIC FIELD CONFIGURATION

Let us now see in more detail how the global magnetic field is affected by the emergence of the flux ropes, and how it evolves past the flux-emergence episode (as defined in Section 4). We will focus on the surface distribution of the magnetic field as a function of time and estimate its consequences for

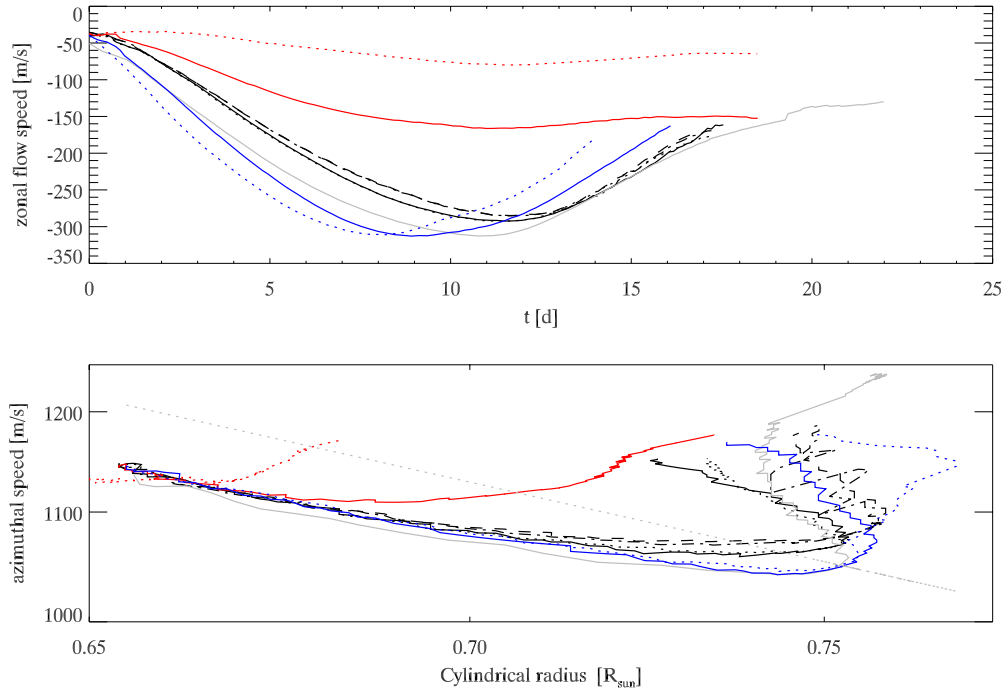


**Figure 18.** Evolution of the zonal (azimuthal) flow generated inside the flux rope as a function of time (top panel) and cylindrical radius (bottom panel) for different runs. The velocity is measured at the axis of the flux rope, which is defined here as the position of the maximum of  $B_\phi$  on the meridional plane. The dotted gray line indicates the slope of a path corresponding to a zonal flow verifying exact angular momentum conservation (inside the flux ropes).

(A color version of this figure is available in the online journal.)

the external field evolution during the emergence episode by means of potential field extrapolations. We will assume in what follows that the extrapolated magnetic field provides a reasonable qualitative indication of the potential component of the coronal field (hence not of the total magnetic field).

### 5.1. Surface Magnetic Field Distribution

We will consider primarily the latitudinal distributions of magnetic field at the surface. Figure 19 shows the temporal evolution of the azimuthally averaged radial and azimuthal magnetic field at the surface of the Sun for different runs as a function of latitude and time. The panel in the figure represents, respectively from the top to bottom rows, the standard case, the case with inverted handedness, the case with inverted handedness and polarity, and the standard flux rope in a hydrodynamical background and the background dynamo run (without flux ropes). The emergence episode initially produces a positive/negative magnetic polarity pair ( $B_r$ , on the left column) and a one-signed signature in  $B_\phi$  (on the right column). Its initial latitudinal extension grows quickly, up to about  $20^\circ$  between  $t = 12$  days (beginning of the emergence episode) and  $t = 15$  days. At this stage, the northernmost limit of the emerged region expands at a rate of about  $2.6 \text{ day}^{-1} \approx 365 \text{ m s}^{-1}$  (which is the slope of the blue line in Figure 19). In the standard case, the positive polarity occupies the northern half of the emerging region and  $B_\phi$  is positive, as expected for the emergence of a right-handed twisted flux rope (see, e.g., Pevtsov et al. 2003; Zhang 2006; Zhang et al. 2012). The remaining cases display symmetric  $B_r$  pairs and/or  $B_\phi$ , according their polarity and handedness. The time–latitude diagrams show that the emerged magnetic flux is transported poleward globally (and not only in the longitude interval shown in Figure 14), and also that its latitudinal extent keeps growing in time. Furthermore, the northern half spreads more strongly than the southern half (the

asymmetry being slightly more pronounced for the right-handed flux ropes). In the case with a hydrodynamical background, this magnetic polarity pattern evolves more smoothly than in the cases with a dynamo background. In all cases, the bipolar pattern is progressively distorted by the surface flows and ends up being disrupted between  $t = 30$  and  $t = 40$  days (compare with the last two columns in Figure 14, showing the surface distribution of  $B_r$ ). The emerged azimuthal magnetic field also displays the same latitudinal spread and disruption patterns. More surprisingly, a strong negative  $B_\phi$  signal appears at the surface at  $t \sim 20$  days in the standard dynamo case and outlives the original  $B_\phi$  signal (with a positive sign). This feature is not introduced by the background dynamo, as it does not appear in the background dynamo run (without flux rope; see bottom row in Figure 19). Moreover, the hydrodynamic (no dynamo) counterpart of the standard case shows the same behavior. The key parameter is the flux-rope’s handedness: all right-handed cases display this behavior, while left-handed flux ropes do not.

The northernmost edge of the emerged region drifts at this moment northward (poleward) at a nearly uniform rate of  $\sim 0.22 \text{ day}^{-1} \approx 30 \text{ m s}^{-1}$  for all cases (yellow line in Figure 19).

### 5.2. Consequences for the External Field

The flux-emergence episodes produce, in our simulations, a strong impact in the global magnetic field topology. In order to make this more evident, in Figure 20 we show two three-dimensional renderings of the magnetic field in the CZ and of the extrapolated field for the standard case and for the case with a right-handed flux rope. The extrapolations were computed from the surface magnetic field (i.e., from the data shown in the first column of Figure 19). The magnetic field lines are represented as continuous lines colored in blue where  $B_r < 0$  and in orange where  $B_r > 0$ . The instant represented is  $t = 25$  days, close

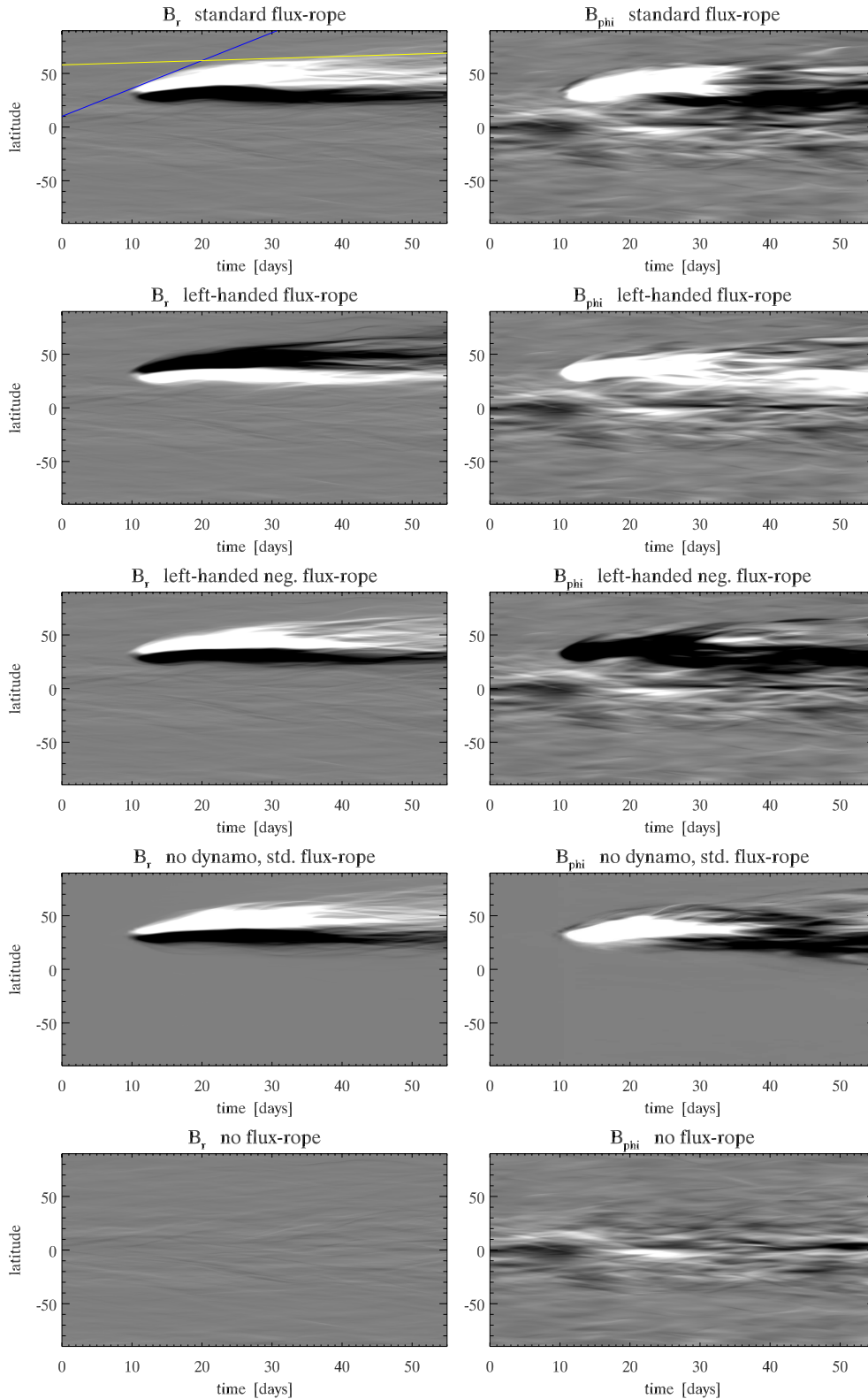


**Figure 19.** “Butterfly” diagrams showing the latitudinal distribution of radial and azimuthal magnetic fields for, respectively from top to bottom, the standard case, the case with inverted handedness, the case with inverted handedness and polarity, the standard flux rope in a hydrodynamical background, and the background dynamo run (without flux ropes). The blue and yellow lines in the upper-left panel indicate, respectively, the poleward drift rates  $2\text{:}6$  and  $0\text{:}22 \text{ day}^{-1}$ .

(A color version of this figure is available in the online journal.)

to the peak in emerged magnetic flux. We clearly see how the overall polarity near the north pole, being strongly influenced by the emerged flux polarity, is different in both the cases. In the low-latitude case, trans-equatorial loops develop and the

impact of the emergence extends over both the hemispheres (not shown in Figure 20; see Figure 22). In all cases, the PILs do not always remain aligned with the azimuthal direction and cover a latitudinal interval of more than 15 deg.

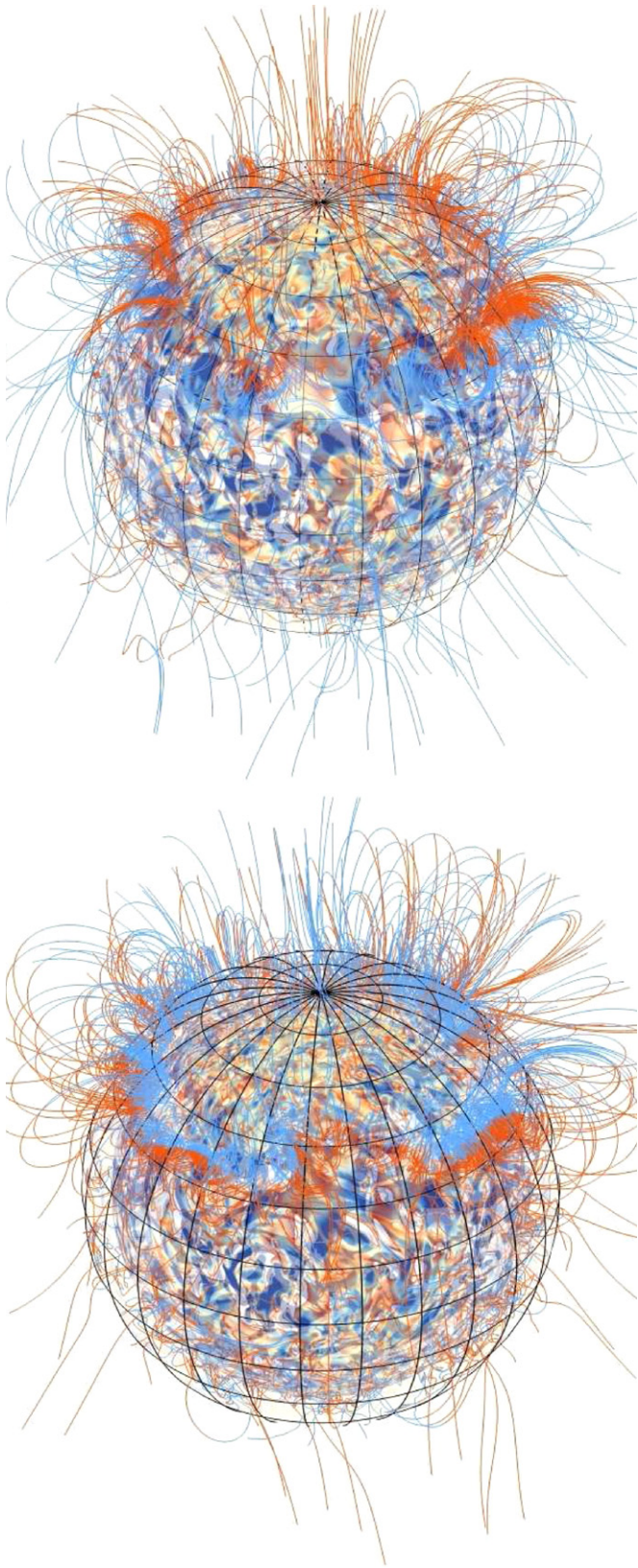


**Figure 20.** Three-dimensional renderings of the magnetic field in the convection zone and the extrapolated magnetic field in the convection zone for the standard case (top) and the case with a right-handed flux rope (bottom), both at  $t = 25$  days. The lines represent magnetic field lines. The surfaces are spherical cuts in the CZ. The colors blue and orange represent, respectively, negative and positive values of  $B_r$ .

(A color version of this figure is available in the online journal.)

Figure 21 shows the geometry of the poloidal axisymmetric component of the coronal field as obtained by potential field extrapolation of the  $\phi$ -averaged surface magnetic field at different instants. The figure shows three time series (one per row) spanning the interval  $t = 5$ –55 days. The top row shows the dynamo run, without a magnetic flux rope. The middle row shows the standard case, and the bottom row shows the case with a flux rope with negative polarity. The color scale represents the radial magnetic field polarity, with  $B_r > 0$  in orange and  $B_r < 0$  in blue. The continuous and dashed lines are magnetic field lines, the former corresponding to CW-oriented magnetic loops and the latter to CCW-oriented loops. Although the coronal magnetic field is not expected to be potential, potential field extrapolations, such as those in Figures 20–22, are known to give a reasonable indication of its global topology, showing the location of the strong/weak flux concentrations and the coronal magnetic connectivity (Wang & Sheeley 2003; Schrijver & DeRosa 2003). The study of the dynamical evolution of the corona requires a different type of approach, based on MHD descriptions or at least on non-potential approximations (e.g., Yeates et al. 2010). Nevertheless, it has been shown that the slowly varying global-scale coronal magnetic field structure is still well reproduced by potential field extrapolations, and that these produce estimates close to those from full MHD models (Riley et al. 2006; Hu et al. 2008). Potential field extrapolations are, therefore, useful tools to elaborate hypotheses on such dynamics and can ultimately be used to initialize time-dependent MHD simulations (e.g., Lionello et al. 2005).

The background dynamo undergoes on its own a short global polarity reversal, taking place between  $t = 20$  days and  $t = 30$  days (see Figure 23 for a more precise depiction). The global external magnetic field is strongly perturbed by the emergence of the flux rope, which can reinforce or completely inhibit this polarity reversal (depending on the flux-rope’s polarity). This is visible in the fourth column of Figure 21 for  $t = 25$  days. The final states for both the cases with flux ropes clearly display inverse polarities in the northern hemisphere, meaning that the emerged flux is indeed substantial compared to the background external field (generated by the dynamo). More precisely, in the standard case the emerged flux contributes to an increase in the global magnetic flux and reinforces the underlying dynamo polarity reversal. The magnetic topology in the northern hemisphere then becomes much simpler than the one due solely to the dynamo field. A strong dipolar feature clearly dominates over the smaller scale higher-order magnetic structures that are visible in the low corona at the initial state. In the southern hemisphere, the influence of the emerged magnetic flux is less dominant. Some topological features resulting from the distribution of surface smaller-scale mixed polarity pairs prevail, such as the pseudo-streamer structure visible at a latitude of  $\sim 45^\circ$  S. In the case with a negative polarity flux rope, the emerged flux completely inhibits the system to undergo a global magnetic polarity reversal. The latitude of emergence plays an important role in the perturbations of the external magnetic field in different ways. Magnetic flux ropes placed at lower latitudes will rise more slowly than high-latitude ones (see Section 3.2 and Figure 9) and hence emerge at different instants. The emerged magnetic field then interacts with different states of the time-dependent background dynamo global field. More specifically, the low-latitude case studied here ( $15^\circ$  N) emerges before the background dynamo reverses its global polarity, while the high-latitude case ( $45^\circ$  N) emerges afterward. Figure 22 shows a snapshot of the poloidal magnetic field (CZ and extrapolated

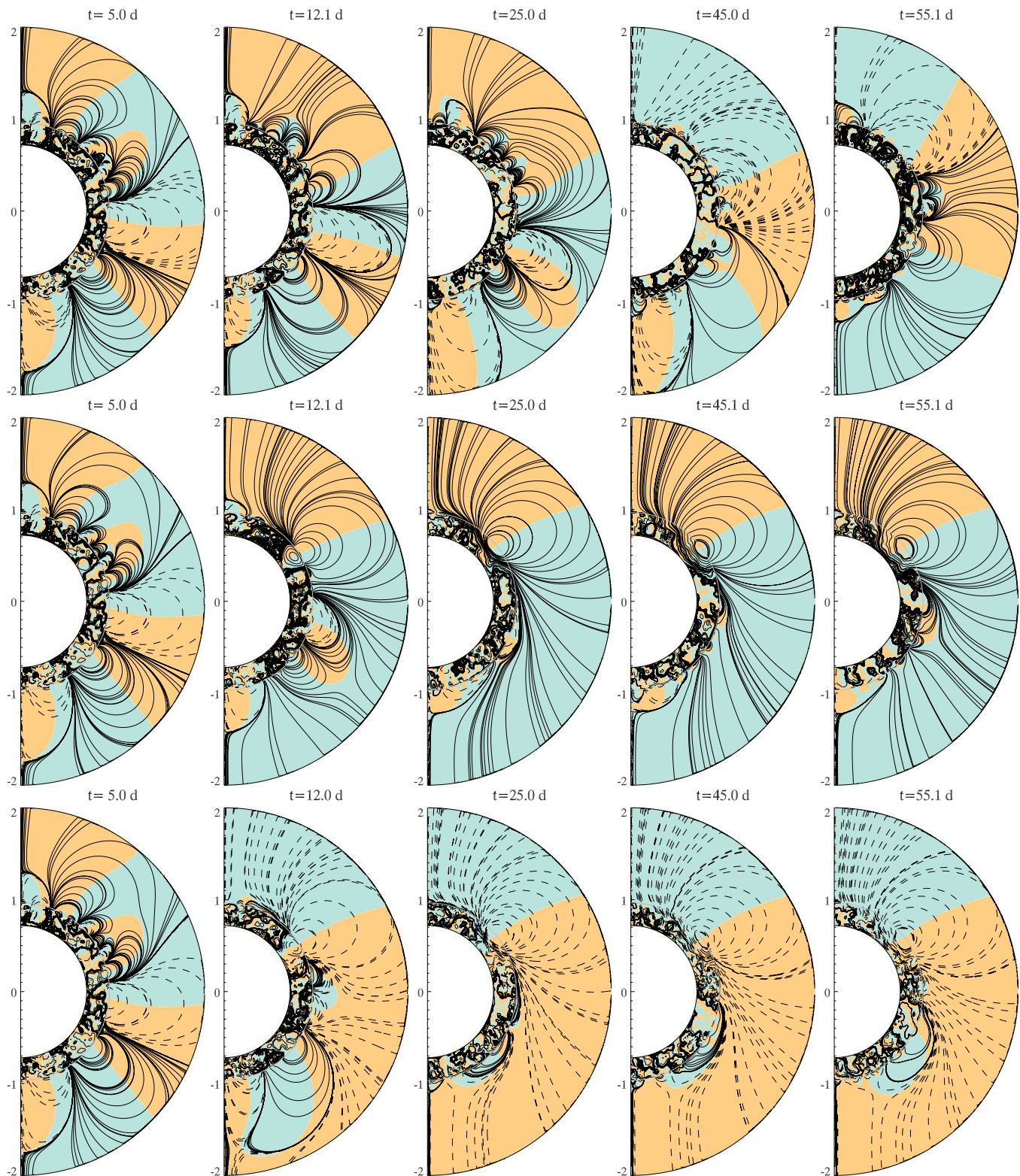


**Figure 21.** Time series of the azimuthally averaged poloidal magnetic field in the CZ and the extrapolated potential field in the corona for the dynamo run without flux rope (top row), for the dynamo row with a standard flux rope (middle row), and for the dynamo run with a flux rope with the inverse polarity (bottom row). The figures show the convective zone (with the light gray curve representing the upper boundary of the numerical domain) and the extrapolated field up to  $2 R_{\odot}$ . Black lines represent magnetic field lines, with continuous and dashed lines representing magnetic loops with opposite chirality (continuous lines correspond to CW-oriented magnetic loops and dashed lines to CCW-oriented loops). Orange and blue tones represent the regions where the radial magnetic field is, respectively, positive and negative.

(A color version of this figure is available in the online journal.)

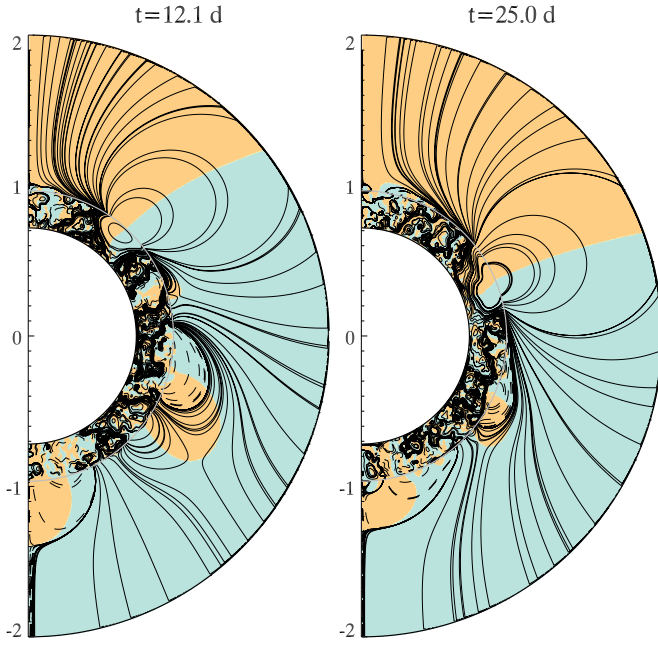


**Figure 22.** Snapshots of the high-latitude and low-latitude cases at the instants  $t = 12$  days and  $t = 25$  days (respectively). These instants correspond roughly to the stage in the evolution of the emergence episode represented in the second column in Figure 21 for the cases at standard latitude.

(A color version of this figure is available in the online journal.)

field) both for the high- and the low-latitude cases. The instants represented were chosen to correspond roughly to the same stage in the evolution of the emergence episode (taking into account the different buoyant rise speeds). The low-latitude flux rope introduces a strong topological perturbation to the external field, spreading well across the equator and into the opposite

hemisphere. The influence of the high-latitude case is more restrained to the hemisphere of emergence. This is not only due to the different distances between the emergence site and the equator. In fact, the total amount of flux-rope-related magnetic flux which crosses the upper boundary depends on the latitude of emergence. Similar flux ropes, with the same cross-section and toroidal magnetic flux, will reach the top of the domain with different azimuthal extents, depending on the latitude of emergence. Hence, the amount of magnetic flux available to cross the surface scales as  $\sin(\theta)$  (ignoring other effects).

It is worth noting that these effects are long lasting; the external magnetic field geometry roughly maintains its newly acquired topology during the post-emergence phases, even though the signs of the emerged flux at the surface are already disappearing (cf. the last column in Figure 14). This supports the idea that much of the magnetic flux involved in the actual process of polarity reversal in the Sun may be carried outward by the emerging AR flux ropes.

Figure 23 shows the signed magnetic flux integrated at the surface over the northern hemisphere as a function of time, which approximates the amplitude of the global solar dipole. The top panel then compares the global dipole polarity of the dynamo run without introduction of a flux rope (long dashed line) and for the strong-field cases with different handedness and polarities (continuous, dotted, and dashed black lines). The bottom panel shows the same curves with the dynamo background run subtracted off. The case with a hydrodynamical background (continuous gray line) is also represented here for comparison. As discussed in the previous paragraph, the background dynamo undergoes, by itself, a short polarity reversal between  $t = 20$  and 30 days. This figure lets us see more quantitatively how in the runs with magnetic flux ropes the emerged flux is sufficient to either reinforce or completely inhibit the polarity inversion. This effect depends only on the flux-rope's own

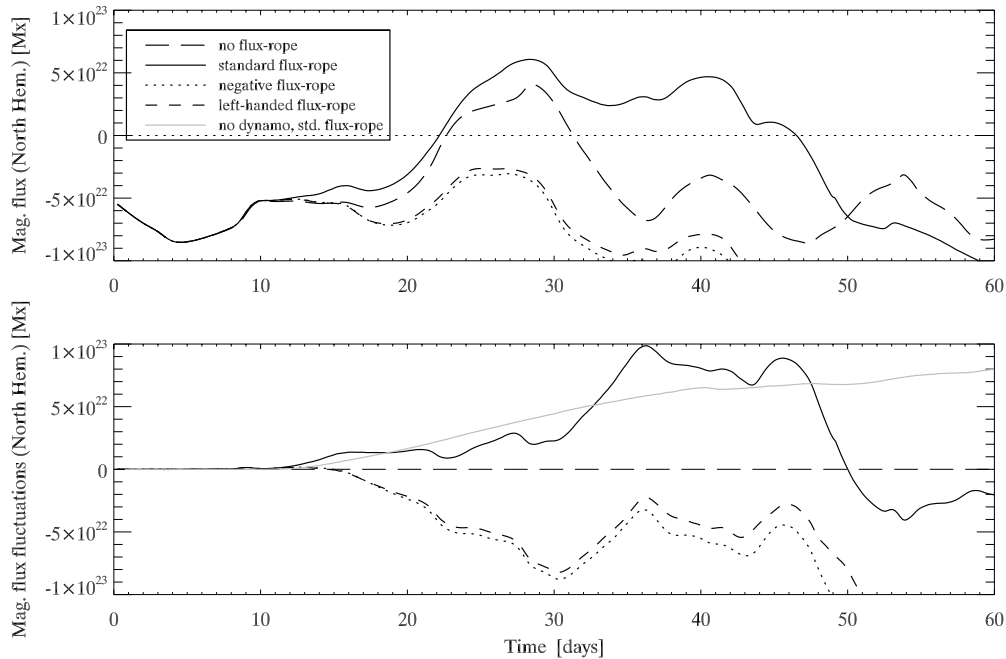


**Figure 23.** Signed magnetic flux  $\int_0^{\pi/2} B_r \cdot dS$  at the surface as a function of time (over the northern hemisphere only). The top panel shows the total magnetic flux, while the bottom panel shows the deviations relative to the run with background dynamo field but no flux rope. The runs represented are the standard case, the cases with opposite polarity and handedness, the hydro case (standard flux rope without dynamo field), and the dynamo run without flux rope. The hydro case is only shown in the second panel. The figure shows that the global polarity of the magnetic field is strongly dominated by the emerged flux in the strong field cases. This is not so much the case for the weaker field cases. The difference between the hydro and standard cases (gray and black continuous lines, respectively) shows that the flux-rope's field interacts with the background dynamo field.

poloidal magnetic polarity; the flux-rope’s handedness is irrelevant. The dotted and dashed curves—which follow each other closely—represent runs setup with the same polarities but opposite handedness. The case featuring a standard flux rope evolving in a hydrodynamical background shows a strikingly simpler behavior associated with a very uniform growth in surface magnetic flux. The background dynamo magnetic flux amplitude reaches a maximum of  $10^{23}$  Mx during the time interval we are considering, with a time-averaged amplitude (rms) of about  $4 \times 10^{22}$  Mx. The maximum contribution of the emerging flux ropes themselves amounts to up to  $10^{23}$  Mx. The total magnetic flux amplitude depends on how both the components (dynamo and emerging flux rope) combine in time. In our simulations, we found a maximum flux amplitude of about  $1.6 \times 10^{23}$  Mx. If the flux rope were to emerge at a different time, we could expect a slightly higher value, closer to  $2 \times 10^{23}$  Mx. These values are on the upper side (but within range) of the observed distributions given by Schrijver & Harvey (1994) and Rempel (2006). Note that our simulations produce an azimuthal activity band rather than individual ARs. The net magnetic flux is then necessarily high, with contributions from a few simultaneous ARs. Also keep in mind that Figure 23 represents only the cases with the strongest  $B_0$  and that the magnetic fluxes reported above correspond to those strong-field cases. The simulation fluxes were computed at  $r = 0.97 R_\odot$ ; the actual photospheric fluxes are likely to be smaller.

As discussed in Section 3.4, Figure 12 (bottom-right panel) shows the total Poynting flux crossing the upper spherical boundary of the domain as a function of time. Note that the sign of Poynting flux is defined such that an outward energy flux is negative in the figure. That is, a negative Poynting flux means electromagnetic energy is being transferred from the CZ to the outside, while a positive flux means the opposite. The figure shows that the whole flux-emergence episode ( $t = 12$ – $20$  days for the standard case) is indeed associated with a strong increase in Poynting flux (into the corona). After the emergence episode, the Poynting flux actually reverses for some time. This time interval corresponds to the third and fourth columns in Figures 14 and 21. The emerged magnetic field is losing its spatial coherence and slowly decaying at this moment.

The maximum amplitude depends strongly on the flux-rope’s strength (scaling roughly as  $B^2$ ). The emerging flux-rope’s handedness also plays a role here. In our runs, left- and right-handed cases show amplitude differences of a factor of 0.1. The polarity of the flux rope (the sign of  $B_\phi$ ), though, is unimportant. The presence of a background dynamo field also conditions the results. The gray curve in Figure 12 represents the evolution of the hydrodynamical background case, for which there are some quantitative differences (specially in the later phases of the emergence episode).

## 6. DISCUSSION AND CONCLUSIONS

The results discussed in the previous sections are based on a series of global-scale numerical simulations using the ASH code to model flux emergence in a spherical convective shell simultaneously possessing differential rotation, meridional flows, and a dynamo-generated magnetic field. We have investigated how buoyant magnetic flux ropes are influenced by a three-dimensional background nonlinear dynamo during their rise through the convection zone and how they contribute to the global magnetic flux budget. Initial position, flux-rope twist, and radius were chosen following the conclusions in Jouve & Brun (2009), who studied the buoyant rise of such magnetic

structures in a fully developed but hydrodynamical CZ. We focused on parameters that relate more directly to the interactions between the flux-rope’s magnetic field and the background dynamo, namely the flux-rope strength, polarity and handedness, and the flux-rope’s initial latitude. This study is, to our knowledge, the first one addressing this problem systematically. Dorch (2007) performed a first step on this direction, but they limited their simulations to Cartesian setups where the background field was fixed and uniform.

Our main results can be summarized as follows:

1. The effects of the interaction between the flux rope and the background magnetic field are negligible in the initial phases of the buoyant rise, but they become progressively more important as the flux ropes evolve. The overall buoyant rise speeds are marginally lower for flux ropes interacting with a background magnetic field than for flux ropes evolving in a purely hydrodynamical convective background. Specific orientations of the flux-rope’s magnetic field lines with respect to the background field can produce large rise velocity disparities. For a given flux-rope configuration, the largest source of buoyant rise speed disparities is the flux-rope initial latitude.
2. The fraction of the flux-rope’s magnetic flux that emerges is large enough to strongly perturb the global topology of the external field. The emerged field is predominantly dipolar and may contribute to enhancing the global dynamo polarity reversal or prevent it from happening. The global magnetic topology remains affected by the emerged flux for a long time—well beyond the period of time during which the surface tracers of flux emergence are visible.
3. The amplitude of the flux-rope’s magnetic field  $B_c$  and density  $\rho_c$  were observed to scale as  $B_c \propto \rho_c^\alpha$  with  $\alpha \lesssim 1$  during the buoyant rise phase. This differs from the results of local-scale simulations of flux emergence in the upper layers of the CZ only (Cheung et al. 2010).
4. The flux rope transports a retrograde zonal (azimuthal) flow, which shows a strong signature at the surface levels. This zonal flow manifests itself as a localized surface shearing whose actual amplitude depends on the latitude at which the flux-rope emerges (due to the difference between the mean differential rotation and the flux-rope’s azimuthal velocity). The shearing amplitude is maximum for low-latitude flux ropes (up to a few hundreds of  $\text{m s}^{-1}$ ), albeit with a limited duration.
5. A set of discontinuous north–south aligned magnetic bipolar patches appear as the buoyant flux ropes reach the top of the domain. These are then sheared and twisted by the surface flows, and the emerged magnetic flux is pushed into the convective cell boundaries. The bipolar patches have an intrinsic magnetic helicity which depends directly on the flux-rope’s polarity and handedness. The helicity’s amplitude and sign changes afterward as a result of the underlying horizontal surface motions, specifically the latitudinal shearing of the mean azimuthal velocity (differential rotation) and vertical vorticity at the latitude of emergence.
6. The bipolar patches first expand quickly as the buoyant flux ropes slow down and come to a complete stop. From then on, this magnetic flux is slowly advected poleward by the underlying meridional flows. The nature of the distribution of the surface magnetic patches varies with the latitude of emergence—the low-latitude cases being particularly patchy (as they rise more slowly and hence are more affected by the interaction with the convective flows).

7. Magnetic flux emergence is preceded by a strong and localized enhancement in  $v_r$  (accompanied by a weaker density increase) at the place where the flux rope will emerge. A sharp current density increase is also observed immediately before the actual flux-emergence episode. Thus, we suggest the following temporal sequence: (1) increase in  $v_r$  and  $\rho$ , (2) sharp increase in  $J^2$ , and (3) increase in magnetic flux amplitude. The exact temporal delays between these diagnostics depend on the specific properties of the emerging flux-rope model, but the ordering seems to be general.
8. The typical double-tailed cross-section for the flux rope is not so clearly found (as in simulations using a hydrodynamical background), because the peripheral magnetic flux is interchanged continuously with the magnetoconvective environment.

All of the points listed above (except points 7 and 8) describe global-scale consequences of the buoyant rise and emergence of magnetic flux ropes, or effects that are affected by the underlying global-scale flow properties. Please note that the top of the numerical domain (the “surface”) is placed at  $0.97 R_\odot$ , and flux-emergence episodes are hence defined here as enhancements of the “surface” magnetic flux related to the arrival of a buoyant flux rope. For these reasons, our estimations concerning surface emergence diagnostics are meant to provide insight into the sub-surface dynamics and flux-emergence processes rather than to produce directly observable features. Also note that we introduced buoyant twisted magnetic flux ropes in pressure equilibrium directly at the base of the CZ with various tunable parameters (twist, location, and amplitude), as the physical mechanisms at the origin of such buoyant magnetic structures are out of the scope of our study (see Nelson et al. 2013). The dynamical evolution of these flux ropes can be described in terms of their buoyant rise speed, trajectory, and interaction with the surroundings alone. The interaction with the multi-scale dynamo magnetic field is at first weak but becomes more and more important as the flux rope rises from the deep layer of the convective envelope to the top of the domain. The added ME is reprocessed by the dynamo, yielding a higher ME than, but similar growth rate to, the reference flux rope free dynamo run.

We performed potential field extrapolations of the surface magnetic fields during the flux-rope buoyant rise, emergence, and post-emergence phases in order to have an idea on how the emerged flux perturbs the external magnetic field. Due to the caveats expressed in Section 2.4, such extrapolations should not be compared with diagnostics of the solar atmosphere.

The emergence episode (that is, from  $t = 12$  to  $t = 20$  days for our standard case) is characterized by the growth of a strongly dipolar magnetic arcade system that disrupts the background multipolar dynamo field. Interestingly, a strong (yet transient) azimuthal flow appears at the surface as the flux-emergence episode proceeds, and this is a source of latitudinal surface shearing. The azimuthal flow is centered right in the middle of the emerging arcades, as it corresponds to a zonal flow carried within the flux ropes. As a result, the shearing is strongest near the boundaries of the emerging region; it is not clear if there is net shearing between opposite footpoints of the arcades.

In the simulation presented in this work, the diffusive coefficients were kept fixed for all runs. An effort should be made in future work to allow these coefficients to be lowered (increasing the turbulence levels in the domain) and to explore different magnetic Prandtl numbers. It would be extremely interesting

to be able to reproduce the flux-rope formation mechanism of Nelson et al. (2011) in simulations like ours. This is to our knowledge still unattainable by the current global convection models rotating at the solar rotation rate, but work is being done to reach that goal, nevertheless. Achieving much lower diffusivities is one of the key aspects of the problem.

Future work will also consider a better description of the photospheric layers (Pinto & Brun 2011) and the presence of multiple buoyant flux ropes in both hemispheres.

This work was supported by ERC Grant No. 207430 (STARS2 project, PI: S. Brun, <http://www.stars2.eu>), the CNRS PNST Interfaces group, and the CNES. Computations were carried out using CNRS IDRIS and CEA’s CCRT facilities (GENCI 1623 project). We would like to thank L. Jouve for useful discussions.

## REFERENCES

- Abbett, W. P., Fisher, G. H., & Fan, Y. 2001, *ApJ*, **546**, 1194
- Archontis, V., & Hood, A. W. 2010, *A&A*, **514**, 56
- Archontis, V., Moreno-Insertis, F., Galsgaard, K., & Hood, A. W. 2005, *ApJ*, **635**, 1299
- Aulanier, G., Démoulin, P., & Grappin, R. 2005, *A&A*, **430**, 1067
- Bannon, P. R. 1996, *JAtS*, **53**, 3618
- Beer, J., Tobias, S., & Weiss, N. 1998, *SoPh*, **181**, 237
- Benevolenskaya, E. E. 2004, *A&A*, **428**, L5
- Browning, M. K., Miesch, M. S., Brun, A. S., & Toomre, J. 2006, *ApJL*, **648**, L157
- Brun, A. S., Antia, H. M., Chitre, S. M., & Zahn, J.-P. 2002, *A&A*, **391**, 725
- Brun, A. S., Miesch, M. S., & Toomre, J. 2004, *ApJ*, **614**, 1073
- Brun, A. S., Miesch, M. S., & Toomre, J. 2011, *ApJ*, **742**, 79
- Brun, A. S., & Toomre, J. 2002, *ApJ*, **570**, 865
- Cameron, R., & Schüssler, M. 2007, *ApJ*, **659**, 801
- Cameron, R. H., & Schüssler, M. 2012, *A&A*, **548**, 57
- Cattaneo, F. 1999, *ApJL*, **515**, L39
- Charbonneau, P. 2010, *LRSP*, **7**, 3
- Cheung, M., Schüssler, M., Tarbell, T. D., & Title, A. M. 2009, in ASP Conf. Ser. 415, *The Second Hinode Science Meeting: Beyond Discovery—Toward Understanding* (San Francisco, CA: ASP), 79
- Cheung, M. C. M., Rempel, M., Title, A. M., & Schüssler, M. 2010, *ApJ*, **720**, 233
- Clune, T. C., Elliott, J. R., Miesch, M. S., Toomre, J., & Glatzmaier, G. A. 1999, *ParC*, **25**, 361
- DeRosa, M. L., Brun, A. S., & Hoeksema, J. T. 2012, *ApJ*, **757**, 96
- Dorch, S. B. F. 2007, *A&A*, **461**, 325
- Emonet, T., & Moreno-Insertis, F. 1998, *ApJ*, **492**, 804
- Fan, Y. 2008, *ApJ*, **676**, 680
- Fan, Y. 2009, *LRSP*, **6**, 4
- Forbes, T. G. 2000, *JGR*, **105**, 23153
- Galsgaard, K., & Nordlund, Å. 1997, *JGR*, **102**, 219
- Gilman, P. A., & Glatzmaier, G. A. 1981, *ApJS*, **45**, 335
- Hanasoge, S., Birch, A., Gizon, L., & Tromp, J. 2012, *PhRvL*, **109**, 101101
- Hood, A. W., & Priest, E. R. 1979, *SoPh*, **64**, 303
- Hu, Y. Q., Feng, X. S., Wu, S. T., & Song, W. B. 2008, *JGRA*, **113**, 03106
- Hughes, D. W., & Falle, S. A. E. G. 1998, *ApJL*, **509**, L57
- Ilionidis, S., Zhao, J., & Kosovichev, A. 2011, *Sci*, **333**, 993
- Işık, E., Schmitt, D., & Schüssler, M. 2011, *A&A*, **528**, 135
- Jones, C. A., & Kuzanyan, K. M. 2009, *Icar*, **204**, 227
- Jouve, L., & Brun, A. S. 2007, *AN*, **328**, 1104
- Jouve, L., & Brun, A. S. 2009, *ApJ*, **701**, 1300
- Jouve, L., Brun, A. S., Arlt, R., et al. 2008, *A&A*, **483**, 949
- Jouve, L., Brun, A. S., & Aulanier, G. 2013, *ApJ*, **762**, 4
- Komm, R., Howe, R., & Hill, F. 2011, *SoPh*, **268**, 407
- Kosovichev, A. G. 2012, *SoPh*, **279**, 323
- Kosano, K., Bamba, Y., Yamamoto, T. T., et al. 2012, *ApJ*, **760**, 31
- Lantz, S. R., & Fan, Y. 1999, *ApJS*, **121**, 247
- Leighton, R. B. 1969, *ApJ*, **156**, 1
- Linton, M. G., Longcope, D. W., & Fisher, G. H. 1996, *ApJ*, **469**, 954
- Lionello, R., Riley, P., Linker, J. A., & Mikić, Z. 2005, *ApJ*, **625**, 463
- Liu, W., Ofman, L., Nitta, N. V., et al. 2012, *ApJ*, **753**, 52
- Martínez-Sykora, J., Hansteen, V., & Carlsson, M. 2008, *ApJ*, **679**, 871
- Martínez-Sykora, J., Hansteen, V., & Carlsson, M. 2009, *ApJ*, **702**, 129

- Miesch, M. S., Brun, A. S., & Toomre, J. 2006, *ApJ*, **641**, 618
- Morel, P. 1997, *A&AS*, **124**, 597
- Nandy, D., Muñoz-Jaramillo, A., & Martens, P. C. H. 2011, *Natur*, **471**, 80
- Nelson, N. J., Brown, B. P., Brun, A. S., Miesch, M. S., & Toomre, J. 2011, *ApJL*, **739**, L38
- Nelson, N. J., Brown, B. P., Brun, A. S., Miesch, M. S., & Toomre, J. 2013, *ApJ*, **762**, 73
- Pevtsov, A. A., Maleev, V. M., & Longcope, D. W. 2003, *ApJ*, **593**, 1217
- Pinto, R., & Brun, S. 2011, in *IAU Symp. 271, Astrophysical Dynamics: From Stars to Galaxies*, ed. N. Brummell, A. S. Brun, Y. Ponty, & M. S. Miesch (Cambridge: Cambridge Univ. Press), 393
- Rempel, M. 2006, *ApJ*, **647**, 662
- Riley, P., Linker, J. A., Mikić, Z., et al. 2006, *ApJ*, **653**, 1510
- Schou, J., Antia, H. M., Basu, S., et al. 1998, *ApJ*, **505**, 390
- Schrijver, C. J., & DeRosa, M. L. 2003, *SoPh*, **212**, 165
- Schrijver, C. J., & Harvey, K. L. 1994, *SoPh*, **150**, 1
- Schrijver, C. J., & Title, A. M. 2011, *JGRA*, **116**, 04108
- Schrijver, C. J., Title, A. M., van Ballegooijen, A. A., Hagenaar, H. J., & Shine, R. A. 1997, *ApJ*, **487**, 424
- Shibata, K., Tajima, T., Steinolfson, R. S., & Matsumoto, R. 1989, *ApJ*, **345**, 584
- Thompson, M. J., Christensen-Dalsgaard, J., Miesch, M. S., & Toomre, J. 2003, *ARA&A*, **41**, 599
- Wang, Y.-M., & Sheeley, N. R. 1991, *ApJ*, **375**, 761
- Wang, Y.-M., & Sheeley, N. R. 2003, *ApJ*, **599**, 1404
- Warnecke, J., Käpylä, P. J., Mantere, M. J., & Brandenburg, A. 2012, *SoPh*, **280**, 299
- Weber, M. A., Fan, Y., & Miesch, M. S. 2011, *ApJ*, **741**, 11
- Weber, M. A., Fan, Y., & Miesch, M. S. 2012, *SoPh*
- Wissink, J. G., Matthews, P. C., Hughes, D. W., & Proctor, M. R. E. 2000, *ApJ*, **536**, 982
- Wong, V. C., & Lilly, D. K. 1994, *PhFl*, **6**, 1016
- Yeates, A. R., Constable, J. A., & Martens, P. C. H. 2010, *SoPh*, **263**, 121
- Zhang, H., Moss, D., Kleorin, N., et al. 2012, *ApJ*, **751**, 47
- Zhang, M. 2006, *ApJL*, **646**, L85